Multi-band analyses of the bright GRB 230812B and the associated SN2023pel

T Hussenot-Desenonges, T Wouters, N Guessoum, I Abdi, A Abulwfa, C Adami, J.F. Agüí Fernández, T Ahumada, V Aivazyan, D Akl, et al.

Monthly Notices of the ROYAL ASTRONOMICAL SOCIETY

MNRAS **530,** 1–19 (2024) https://doi.org/10.1093/mnras/stae503
Advance Access publication 2024 March 18

Multiband analyses of the bright GRB 230812B and the associated SN2023pel

T. Hussenot-Desenonges,[1★] T. Wouters,[2,3] N. Guessoum ,[4★] I. Abdi,[4] A. Abulwfa,[5] C. Adami,[6] J. F. Agüí Fernández ,[7] T. Ahumada,[8] V. Aivazyan,[9,10] D. Akl,[4] S. Anand ,[8] C. M. Andrade,[11] S. Antier ,[12★] S. A. Ata,[5] P. D'Avanzo,[13] Y. A. Azzam,[5] A. Baransky,[14] S. Basa,[6] M. Blazek,[15,16] P. Bendjoya,[17] S. Beradze,[9,10] P. Boumis,[18] M. Bremer,[19] R. Brivio,[13,20] V. Buat,[6] M. Bulla,[21,22,23] O. Burkhonov,[24] E. Burns,[25] S. B. Cenko,[26,27] M. W. Coughlin,[11] W. Corradi,[28] F. Daigne,[29] T. Dietrich,[30,31] D. Dornic,[32] J.-G. Ducoin,[29,32] P.-A. Duverne,[33] E. G. Elhosseiny,[5] F. I. Elnagahy,[5] M. A. El-Sadek,[5] M. Ferro,[13,20] E. Le Floc'h,[34] M. Freeberg,[35] J. P. U. Fynbo,[36,37] D. Götz,[34] E. Gurbanov,[38] G. M. Hamed,[5] E. Hasanov,[38] B. F. Healy,[39] K. E. Heintz,[36,37] P. Hello,[1] R. Inasaridze,[9,10] A. Iskandar,[40] N. Ismailov,[38] L. Izzo,[41,42] S. Jhawar,[30] T. Jegou du Laz,[43] T. M. Kamel,[5] S. Karpov,[15] A. Klotz,[44,45] E. Koulouridis,[18] N. P. Kuin,[46] N. Kochiashvili,[9] S. Leonini,[47] K.-X. Lu,[48] D. B. Malesani,[36,37,49] M. Mašek,[50] J. Mao,[48,51,52] A. Melandri,[13,53] B. M. Mihov,[54] R. Natsvlishvili,[9] F. Navarete,[55] V. Nedora,[31] J. Nicolas,[12] M. Odeh,[12] J. Palmerio,[56] P. T. H. Pang,[2,3] M. De Pasquale,[57] H. W. Peng,[58] S. Pormente,[12] J. Peloton,[1] T. Pradier,[59] O. Pyshna,[14] Y. Rajabov,[24] N. A. Rakotondrainibe,[6] J.-P. Rivet,[17] L. Rousselot,[12] A. Saccardi,[56] N. Sasaki,[28] B. Schneider,[60] M. Serrau,[61] A. Shokry,[5] L. Slavcheva-Mihova,[54] A. Simon,[62,63] O. Sokoliuk,[14,64] G. Srinivasaragavan,[26,27,65] R. Strausbaugh,[66] A. Takey,[5] N. R. Tanvir,[67] C. C. Thöne,[68] Y. Tillayev,[24,69] I. Tosta e Melo,[70] D. Turpin,[34] A. de Ugarte Postigo,[6,12] V. Vasylenko,[62,63] S. D. Vergani,[56] Z. Vidadi,[38] D. Xu,[52] L. T. Wang,[40] X. F. Wang,[58,71] J. M. Winters,[19] X -L. Zhang[48] and Z. Zhu[52,72]

Affiliations are listed at the end of the paper

Accepted 2024 February 13. Received 2024 February 7; in original form 2023 October 22

ABSTRACT

GRB 230812B is a bright and relatively nearby ($z = 0.36$) long gamma-ray burst (GRB) that has generated significant interest in the community and has thus been observed over the entire electromagnetic spectrum. We report over 80 observations in X-ray, ultraviolet, optical, infrared, and submillimetre bands from the GRANDMA (Global Rapid Advanced Network for Multimessenger Addicts) network of observatories and from observational partners. Adding complementary data from the literature, we then derive essential physical parameters associated with the ejecta and external properties (i.e. the geometry and environment) of the GRB and compare with other analyses of this event. We spectroscopically confirm the presence of an associated supernova, SN2023pel, and we derive a photospheric expansion velocity of $v \sim 17 \times 10^3\,\mathrm{km\,s^{-1}}$. We analyse the photometric data first using empirical fits of the flux and then with full Bayesian inference. We again strongly establish the presence of a supernova in the data, with a maximum (pseudo-)bolometric luminosity of $5.75 \times 10^{42}\,\mathrm{erg\,s^{-1}}$, at $15.76^{+0.81}_{-1.21}$ d (in the observer frame) after the trigger, with a half-max time width of 22.0 d. We compare these values with those of SN1998bw, SN2006aj, and SN2013dx. Our best-fitting model favours a very low density environment ($\log_{10}(n_{\rm ISM}/\mathrm{cm^{-3}}) = -2.38^{+1.45}_{-1.60}$) and small values for the jet's core angle $\theta_{\rm core} = 1.54^{+1.02}_{-0.81}$ deg and viewing angle $\theta_{\rm obs} = 0.76^{+1.29}_{-0.76}$ deg. GRB 230812B is thus one of the best observed afterglows with a distinctive supernova bump.

Key words: methods: statistical – techniques: photometric – techniques: spectroscopic – gamma-ray burst: individual: GRB 230812B – gamma-ray bursts – transients: supernovae.

★ E-mail: nguessoum@aus.edu (NG); sarah.antier@oca.edu (SA); thomas.hussenot@ijclab.in2p3.fr (THD)

1 INTRODUCTION

Gamma-ray bursts (GRBs) are energetic explosions that, with their afterglows, emit over the entire range of electromagnetic radiation. Typically, they are classified in two categories: 'long' (duration), lasting more than 2 s in the gamma/X-ray bands, and 'short', lasting less than 2 s. Long GRBs are widely believed to result from the collapse and explosion of a very massive star, hence they are often referred to as 'collapsar' and hypernova. Short GRBs are thought to result from the merger of a neutron star with another neutron star or with a black hole (compact objects). In both categories, GRBs produce bipolar jets emerging from the newly formed compact object. The jets interact with the surrounding matter and, through shocks, producing 'afterglow' emission, first in the X-ray band, then, as the jet slows and weaker shocks occur, UV, optical, IR, and radio emissions. The luminosity of GRB afterglows is moderately correlated with the isotropic prompt-emission (mostly γ-ray) energy released, $E_{\rm iso}$ (Gehrels et al. 2008; Nysewander, Fruchter & Pe'er 2009; Kann et al. 2010, 2011).

Core-collapse GRBs are also associated with an optical/near-infrared supernova (SN), which represents the more isotropic outburst (in addition to the jet) from the central explosive process (more below). GRB 980425/SN1998bw was the first well-documented example of a GRB associated with a supernova, a core-collapse event strongly associated with a (long-duration) burst (Galama et al. 1998; Patat et al. 2001). The association between SN1998bw and GRB 980 425 was first made from the optical spectrum and location of a transient in a spiral arm of the galaxy ESO184-G82 (Galama et al. 1998). Observations of such cases strengthen the fact that galaxies with strong star formation have greater potential for the occurrence of long gamma-ray bursts (Bloom, Kulkarni & Djorgovski 2002).

In addition to this seminal case, a number of similar associations have been observed since then, such as GRB 030 329 with SN2003dh (Hjorth et al. 2003; Stanek et al. 2003). Spectral features of SN2003dh indicated a very massive star origin (Deng et al. 2005), reinforcing the notion that the GRB resulted from a core-collapse process. These breakthrough observations opened the door for the collection of a significant number of GRB-SN associations, now a well-identified class of astrophysical events. Other thoroughly studied examples include GRB 031203/SN2003lw (Malesani et al. 2004), GRB 060218/SN2006aj (Ferrero et al. 2006; Pian et al. 2006), GRB 100316D/SN2010bh (Cano et al. 2011), GRB 120422A/SN2012bz (Melandri et al. 2012; Schulze et al. 2014), GRB 130702A/SN2013dx (D'Elia et al. 2015; Mazzali et al. 2021), GRB 161219B/SN2016jca (Ashall et al. 2019), and GRB 171010A/SN2017htp (Melandri et al. 2019).

Important elements which strengthen the association of supernovae with gamma-ray bursts (such as the above cases) include the broad lines in the object's emission spectrum, which are strongly typical of Type Ic supernova lines, and the association with star-forming galaxies; such indicators provide a coherent scenario for the GRB-SN association. Still, important issues remain to be resolved, including: in which cases does a process (collapsar, merger) produce a long or short GRB, and what are their counterparts (r-process or not?); what powers the central engine in each case (magnetar, radioactive heating, etc.); what kinds of jets are produced, etc. To address such key questions, we need a large sample of GRB events exhibiting multiband emission with a (supernova/kilonova) bump in the light curve, characteristic lines in the spectrum, rich enough data to give us constraints on the current models (radioactive heating, millisecond magnetar central engine, etc.).

Important parameters that characterize the SNe associated with GRBs include their maximum luminosity (bolometric and in various bands), the time of their peak emission, and the width at half-max of the light curve. Many authors often use the (less physically meaningful) relative brightness factor k (typically compared to SN1998bw) and the (time) 'stretch factor' s (that is, a 'time width'), also compared to SN1998bw (Cano et al. 2017). A grading system, introduced by Hjorth & Bloom (2012), became widely adopted for characterizing the strength of a GRB-SN association. The grading ranges from (A), very strong (conclusive spectroscopic evidence), to (E), the weakest associations. In the last 25 yr, there have been a dozen cases rated A or A/B (Cano et al. 2017). For those, the average peak time (in the rest frame) is $\sim$13.2 d, with a standard deviation of $\sim$2.6 d (computed from table 3 of Cano et al. 2017).

However, the massive star origin for all long GRBs has recently been challenged by the discovery of a few long GRBs (GRB 211211A, GRB 230307A) associated with a kilonova, normally the signature of a binary compact object merger (Rastinejad et al. 2022; Troja et al. 2022; Yang et al. 2022; Bulla et al. 2023; Levan et al. 2023). In addition to these recent associations with kilonovae, there are also nearby long GRBs without a detected bright SN (Fynbo et al. 2006; Gal-Yam et al. 2006; Gehrels et al. 2006; Valle et al. 2006; Jin et al. 2015). This evidence then produces a more nuanced picture: while most long GRBs originate in massive star explosions, a few may have a different origin. It is thus crucial to obtain a revised census of the collapsar/merger origin for long GRBs. Events at low redshift ($z \lesssim 0.5$) offer an excellent opportunity to carry out this measurement, as the associated SNe, if present, can be easily detected in photometry and even confirmed spectroscopically with 10 m-class telescopes. GRB 230812B provided us with an opportunity to further explore these GRB-Supernova/Kilonova associations.

GRB-SN associations may also be found serendipitously with optical wide-field survey programmes (Soderberg et al. 2008; Sanders et al. 2012) rather than by following bursts and their afterglows. GRB 230812B was initially detected by the *Fermi* Gamma-ray Burst Monitor (GBM – Meegan et al. 2009), the Gravitational wave high-energy Electromagnetic Counterpart All sky Monitor (GECAM), the AGILE/MCAL instrument (Casentini et al. 2023), and the Konus-Wind instrument (Frederiks et al. 2023). This GRB is the most recent event to exhibit a clear SN feature.

Triggered at T_0 = 18:58:12 UT on 2023 August 12 (GBM trigger 713559497/230812790 – Fermi GBM Team 2023), the GRB's light curve in the [10–10 000] keV band showed a very bright short pulse with a T_{90} duration (90 per cent of its fluence at [50, 300] keV) equal to 3.264 $\pm$ 0.091 s (Roberts et al. 2023). The GECAM light curve reported a value of $T_{90} = 4$ s in the [6–1000] keV range (Xiong et al. 2023), and Konus a total time of $\sim$ 20 s in the [20–1200] keV range (Frederiks et al. 2023), consistent with GBM's value.The *Fermi* Large Area Telescope (LAT) independently detected high energy photons with a maximum of 72 GeV (T_0 + 30 s) (Scotton et al. 2023).

With the sky localization probability area provided by GBM or LAT (Lesage et al. 2023; Scotton et al. 2023), a series of tiled observations were obtained by the *Neil Gehrels Swift* observatory X-ray telescope (XRT) (Gehrels et al. 2004), the Zwicky Transient Facility (Salgundi et al. 2023), and the Global MASTER-Net (Lipunov et al. 2023a). The X-ray and UV counterpart of GRB 230812B was discovered 7.1 h after T_0 by *Swift*/XRT (Page & Swift-XRT Team 2023) and *Swift*/UVOT (Kuin & Swift/UVOT Team 2023). The optical counterpart of GRB 230812B was found by the Zwicky Transient Facility on 2023 August 13 at 03:34:56, 8.5 h after the GRB trigger time T_0 (Salgundi et al. 2023), and also by KAIT (the Katzman Automatic Imaging Telescope – Zheng, Filippenko & KAIT GRB team 2023), which provided localization with arcsecond accuracy. Simultaneously, the Global MASTER-Net

robotic telescopes network reported the optical counterpart at the same location (Lipunov et al. 2023b).

A series of photometric observations across the full electromagnetic spectrum were conducted in the months following the trigger. Among them, we can cite as an example the Multi-purpose InSTRument for Astronomy at Low-resolution spectra-imager (T193/MISTRAL) in optical (Amram et al. 2023; Adami et al. 2023a, b), the Italian 3.6 m TNG telescope in near-infrared, and the Northern extended millimeter array (NOEMA) in radio (de Ugarte Postigo et al. 2023b). Spectroscopic observations were also conducted in parallel. It led to the measurements of the transient's redshift: $z = 0.360$ (de Ugarte Postigo et al. 2023a). Twelve days later, observations using OSIRIS+ mounted on the Gran Telescopio Canarias (GTC) showed features in the spectrum characteristic of a GRB-SN event and matched with the spectrum of SN1998bw, indicating, rather conclusively, the presence of a supernova (Agui Fernandez et al. 2023; Agüí Fernández et al. 2023).

Observations with GRANDMA (Global Rapid Advanced Network for Multimessenger Addicts: Antier et al. 2020a, b; Aivazyan et al. 2022; Kann et al. 2023) observatories started on 2023 August 8-13T13:34:22, 0.77 d after T_0, and lasted for 38 d (Mao et al. 2023; Pyshna et al. 2023). In total, more than 20 professional telescopes and several amateur telescopes imaged the source.

GRB 230812B being a high-luminosity and (relatively) close-by burst (z= 0.36) makes it a very worthwhile target of investigation of the GRB and its afterglow, the SN features, and the correlations between the two. To compute distances, absolute magnitudes from apparent magnitudes, etc., we use the `Planck18` cosmological model from `astropy` (Planck Collaboration VII 2020); it adopts a flat cosmology with $H_0 = 67.66$ km s^{-1} Mpc^{-1} and $\Omega_m = 0.310$. The observed redshift $z = 0.360$ then corresponds to a luminosity distance of 1981 Mpc; with the fluence 2.52×10^{-4} erg cm^{-2} given by *Fermi*/GBM (Roberts et al. 2023), we obtain the total isotropic gamma energy $E_{\gamma,\rm iso} = 1.2 \times 10^{53}$ erg; and with the duration (T_{90} = 3.26 s) we get the mean gamma-ray isotropic luminosity $L_{\gamma,\rm iso} = (1+z)E_{\gamma,\rm iso}/T_{90} = 4.9 \times 10^{52}$ erg s^{-1}. This makes this event one of the most luminous GRB-SN events ever recorded.

In this paper, we report observations by the GRANDMA network and its partners of the bright GRB 230812B and the supernova (named SN2023pel) that emerged in the light curve about five days after the burst onset. In Section 2, we present the observational data from more than two dozen instruments and the photometric methods we use. We also explore properties from the host galaxy (brightness, line-of-sight extinction). In Section 3, we analyse our multi-epoch spectra from the GRB afterglow to the confirmation of the presence of SN2023pel. In Section 4, we present the methods we applied in the analysis of the afterglow light curves, using both empirical fits and Bayesian inference. We then present our results on the astrophysical scenarios and processes using different jet structures that best describe the data, and compare SN properties with other GRB-associated supernovae. In Section 5, we present some general discussion and conclusions.

2 OBSERVATIONAL DATA

2.1 *Swift* XRT, UVOT

The X-ray light curve (0.3–10 keV) of GRB 230812B was acquired from the UK *Swift* Science Data Centre[1] (Evans et al. 2007, 2009). The data were extracted from the Burst Analyser[2] (Evans et al. 2010), which provides the light curves and spectra of the [0.3–10] keV apparent flux, as well as the unabsorbed flux density at 10 keV in Jansky units. For the spectral energy distribution (SED) fitting to measure the dust from the galaxy (see sections below), the [0.3–10 keV] XRT data were grouped by 10 counts/bin using `grppha`, a subpackage from HEASOFT (version 6.31.1), for statistical purposes. For the other analyses, we performed a re-binning of the unabsorbed light curve at 10 keV by dividing the observations into eight non-continuous time windows. Among these, four windows contained a cluster of observations occurring within an hour or less, while the remaining four had a single data point each. For each cluster, we computed the mean value and standard deviation to produce data points in the light curve for the analysis. These values are reported in Table A1.

We retrieved images taken by the Ultraviolet/Optical Telescope (UVOT; Roming et al. 2005) from the *Swift* archive.[3] The source was imaged using the broad-band *white* filter from 0.3 to 8.2 d. In all the images, we checked the effectiveness of the aspect correction. To address the excess broadening induced by pointing jitter from the aging attitude control system (Cenko 2023), a meticulous assessment of an early image was conducted to determine where the source counts merge into the background. To accommodate this, a slightly larger aperture of 7.5 arcsec was used for the source. All further images show that the source is contained in this aperture. Background measurements were obtained by analysing an annular region extending from 10 to 22 arcsec (after a careful background region positioning). The later images were summed to get a good signal-to-noise ratio in the usual way using the `Ftool uvotmaghist`.[4] We then transformed the Vega magnitudes to AB magnitudes by adding 0.8 mag as is appropriate in *white* (Breeveld et al. 2011).

The late-time magnitude upper limits suggest that the host galaxy magnitude is faint, *white* >23.2. We tried deriving a near-UV magnitude for the host galaxy from earlier observations from the *Galex gPhoton* database (Million et al. 2016),[5] but were unsuccessful in avoiding contamination by nearby stars. We eventually chose the magnitude 23.54 ± 0.84 in u-band from the Sloan Digital Sky Survey DR7 (Abazajian et al. 2009) as an approximation of the *white* contribution, making sure we propagated properly its very conservative error bars through flux subtraction. The UVOT values, corrected from this constant galaxy flux contribution and from Milky way extinction (see below), are reported in Table A2.

2.2 Optical data set

We conducted simultaneous observations with GRANDMA (Antier et al. 2020a), thanks to its operational platform SKYPORTAL (Coughlin et al. 2023), and with associated partners, from less than a day after the trigger time T_0 up to 38 d (see Fig. 1). Details on the observational campaign in the various networks can be found in the Appendix. From the images taken, we successfully extracted the photometry of the source and corrected it from the constant flux contribution of the host galaxy and from absorption by dust along the line of sight. The data set can be found in Table A2. Our preliminary analysis of the GRANDMA observations has been reported publicly in the General Coordinates Network (GCN)[6] (Mao et al. 2023; Pyshna et al. 2023).

[1] https://www.swift.ac.uk/

[2] https://www.swift.ac.uk/burst_analyser/00021589/

[3] https://swift.gsfc.nasa.gov

[4] https://heasarc.gsfc.nasa.gov/ftools/

[5] https://github.com/cmillion/gPhoton/blob/master/docs/UserGuide.md

[6] https://gcn.nasa.gov/

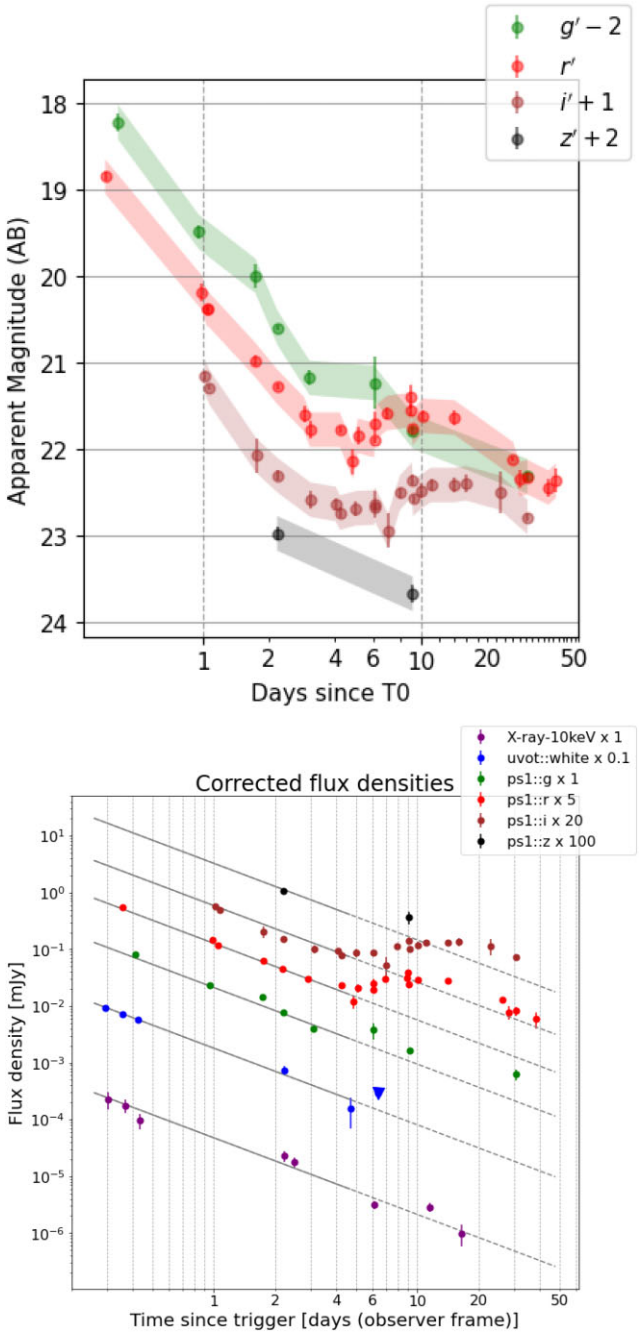

Figure 1. Top: Observations from this work in *g*-, *r*-, *i*-, and *z*-band (observer frame times). Apparent magnitudes before correction by host galaxy flux or for the Milky Way foreground extinction; coloured filled regions with arbitrary errorbars 0.2 mag wide have been added to ease the visualization of the light curves. Bottom: Multiband (X-ray to IR) light curves, corrected from host galaxy flux and the Milky Way foreground extinction. In grey are power laws fit to the data points up to $T_0 + 5$ d (see Section 4.1).

2.2.1 *Photometry*

Prior to photometry, all images were pre-processed in a telescope-specific way with bias and dark subtraction and flat-fielding. We manually masked the regions of the images containing significant imaging artefacts or regions not fully corrected by the pre-processing. Also, we derived astrometric solutions for the images where telescope pipelines did not provide them by using the Astrometry.net service (Lang et al. 2010).

In order to increase the signal-to-noise ratio of the images, we resampled and coadded individual frames using the SWARP software (Bertin 2010) for sequences of images acquired on the same telescope within a short interval of time. Then, we performed the forced photometry at the transient position using STDPIPE (Karpov 2021), a set of Python codes for performing astrometry, photometry, and transient detection tasks on optical images, in the same way as Kann et al. (2023).

In order to simplify the analysis and quality checking of the heterogeneous set of images from different telescopes, and to keep track of the results, we created a dedicated web-based application, STDWEB,[7] which acts as a web interface to the STDPIPE library and provides a user-friendly way to perform all steps of its data processing, from masking bad regions to image subtraction, with thorough checking of the intermediate results of every step, and then adjusting the settings in order to acquire optimal photometry results. It also contains some heuristics for the selection of an optimal aperture radius and an optimal selection of reference photometric catalogue, refining the astrometric solution as needed, etc.

Specifically, for the photometry on all images, we used an aperture radius equal to the mean full-width at half-maximum (FWHM) value estimated over all point-like sources in each image. For photometric calibration, we used the Pan-STARRS DR1 catalogue (Flewelling et al. 2020) for processing the images acquired in filters close to the Sloan system. We used a spatially variable photometric zero-point model represented as a second-order spatial polynomial in order to compensate for the effects of improper flat-fielding, image vignetting, and positionally dependent aperture correction (e.g. due to PSF shape variations). We first performed the analysis taking into account the linear colour term (using $g - r$ for Sloan-like filters) in order to assess how much the individual photometric system of the image deviates from the catalogue one. Then, if the colour term is negligible (e.g. smaller than 0.1), we re-run the analysis of the image without the colour term, thus directly deriving the measurement in catalogue photometric system. If the colour term is significant, we kept it in the analysis and corrected the measurement using the known colour of the transient.

When the signal-to-noise ratio obtained with the forced photometry is below 5, we derive an upper limit for it by multiplying the background noise inside the aperture by 5, and converting this flux value to magnitudes. For images taken too close to each other (on a logarithmic time-scale), we only selected the one with the best signal-to-noise ratio. Images with a sensitivity too low (>1.5 apparent magnitude brighter than nearby measurements) were excluded from the data analysis. Images which, after subtraction of the galaxy's constant flux, give a larger error bar than 0.5, were also excluded from our data set for this analysis.

In parallel, the image reduction for *J* and *K* bands was carried out using the *jitter* task of the ESO-eclipse package.[8] Astrometry was performed using the 2MASS[9] catalogue. Aperture photometry was performed using the Starlink PHOTOM package.[10] To minimize any systematic effect, we performed differential photometry with respect to a selection of local isolated and non-saturated reference stars from the UKIDSS[11] survey.

[7] Accessible at http://stdweb.favor2.info
[8] https://www.eso.org/sci/software/eclipse/
[9] https://irsa.ipac.caltech.edu/Missions/2mass.html
[10] http://www.starlink.ac.uk/docs/sun45.htx/sun45.html
[11] http://www.ukidss.org/

Table 1. Apparent magnitudes of the host galaxy used for flux subtraction and the Milky Way (MW) extinction in the line of sight in different filters.

Filter	Host galaxy contribution		MW extinction
	Magnitude	Error	
u: *white*	23.54 (AB)	0.84	0.099
g'	23.78 (AB)	0.12	0.077
r'	22.83 (AB)	0.10	0.053
i'	22.54 (AB)	0.12	0.040
z'	22.34 (AB)	0.12	0.029
J	21.82 (AB)	0.32	0.017
K	–		0.007

2.2.2 *Host galaxy properties*

The host galaxy of GRB 230812B is SDSS J163631.47+475131.8, with measurements available in SDSS DR16 (Ahumada et al. 2020), but its photometry there is marked as unreliable. The host galaxy's redshift $z = 0.36$ was determined through GTC spectroscopic observations of emission lines (de Ugarte Postigo et al. 2023a). We studied its brightness, both for host flux subtraction and spectral analysis.

Constant flux from the host at the location of GRB 230812B – To better characterize the host galaxy flux, we acquired the data for the GRB position from archival Pan-STARRS DR1 (Waters et al. 2020) images in i' filters, and from the DESI Legacy Surveys DR10 (Dey et al. 2019) stacked image in g', r', and z' filters. We then performed forced photometry on these images, on the same apertures and with the same parameters as used above for the reduction of the data set. To convert Legacy Survey measurements to the Pan-STARRS photometric system, we estimated the colour term[12] while calibrating these images. For the g' filter, this happened to be negligible, but for r' and z', we used the following equations:

$$r' - 0.11 * (g' - r') = 22.73 \pm 0.07$$
$$z' - 0.11 * (r' - i') = 22.31 \pm 0.11,$$

where the magnitudes g', r', i', z' correspond to the Pan-STARRS system. To extract r' and z', we used the g' values estimated from the Legacy Survey image, and i' values from Pan-STARRS image. The results are summarized in Table 1. These host flux contributions were then subtracted from the apparent flux to obtain the transient flux, combining the flux errors from the apparent magnitude and the host contribution to obtain the errors on the host-subtracted flux.

In *J* and *K* filters, there are to our knowledge no NIR detections of the host in available survey catalogues. We obtained a deep late-time *J*-band observation at $T_0 + 60$ d using the TNG telescope, finding a magnitude of 20.91 ± 0.32 (Vega), i.e. 21.82 (AB). This approximate host galaxy contribution could then be subtracted from the other TNG *J* images. Unfortunately, no late-time imaging in *K*-band could be performed, so no host contribution could be estimated in this filter.

Star formation rate from the host galaxy – Using these host flux contributions as approximations for the observed magnitude of the galaxy as a whole, we apply the CIGALE[13] code (Boquien et al. 2019) to study the spectral energy distribution (SED) of the galaxy. This analysis constrains the model parameter space to a mass $M = (1.99 \pm 0.54) \times 10^9\,\mathrm{M}_\odot$, a star formation rate (on the last 10 Myr) $\mathrm{SFR} = 0.17 \pm 0.07\,\mathrm{M}_\odot\mathrm{yr}^{-1}$, and an attenuation $A_V = 0.09 \pm 0.06$ mag. We show the best-fitting spectrum in Fig. 2. However, one should keep in mind that we are effectively considering the flux of the host galaxy within the aperture size of the transient (a few arcseconds because of point spread of the instruments; to be compared with the 5 kpc arcsec^{-1} scale at $z \simeq 0.36$), and are thus missing a fraction of the galaxy, underestimating the flux by an unknown amount that may bias these galaxy parameters. The SFR is especially hard to constrain without more UV data, so its uncertainty provided here is likely underestimated.

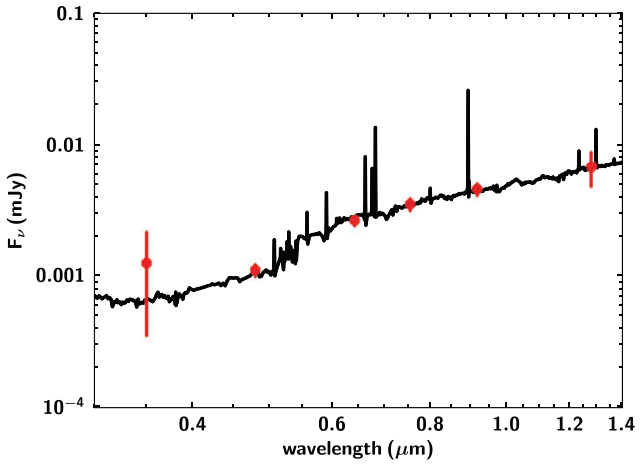

Figure 2. Spectrum of the best-fitting host galaxy model in CIGALE, constrained by our estimations in *ugriz* and *J* bands.

2.2.3 *Line-of-sight extinction*

Milky Way (MW) extinction: We corrected the UV, *griz*, *J*, and *K* bands from the MW extinction values from Schlafly & Finkbeiner (2011), computed along the line of sight by the NED calculator.[14] These corrections are reported in Table 1.

Host galaxy dust extinction: To estimate the extinction suffered by the afterglow due to the host galaxy dust, we created a spectral energy distribution (SED) from X-ray to optical at two epochs: $T_0 + 2.2$ d, corresponding to the quasi-simultaneity of the *whitegriz* bands, and at $T_0 + 4$ d, to include observations from the *J, K* bands; as no quasi-simultaneous observation was available at this epoch for *griJ*, the photometric points were estimated through interpolations. We considered the typical extinction curves of MW, Large Magellanic Cloud, and Small Magellanic Cloud of Pei (1992), which gave similar results.

We report the results obtained with the average SMC dust extinction law. For each epoch, the intrinsic spectrum was modelled with a single or broken power law using the afterglow theory outlined in Sari, Piran & Narayan (1998). For the broken power law, the difference in slope between X-ray and NIR wavelengths was set to $\Delta\beta = \beta_X - \beta_o = 0.5$, which corresponds to the change in slope due to the cooling break. For both epochs, the best fit of the X-ray/NIR SED is obtained with a single power law, and the measured dust extinction A_V is compatible with zero (see Table 2). The higher uncertainty in A_V for $T_0 + 4$ d is due to higher uncertainties in the *J*- and *K*-band observed fluxes. The best fits of the SED at both epochs are shown in Fig. 3.

[12] The colour term *C* here defines the instrumental photometric system through catalogue magnitude and colour as $m_{\mathrm{instr}} = m_{\mathrm{cat}} + C \cdot \mathrm{colour}_{\mathrm{cat}}$ and may be fitted during the photometric calibration of the image.

[13] https://cigale.lam.fr/

[14] http://ned.ipac.caltech.edu/forms/calculator.html

Table 2. Results of the spectral analysis for both epochs.

Epoch	A_V (mag)	β	χ^2 (dof)
$T_0 + 2.2$ d	0.0 ± 0.075	0.710 ± 0.027	19.269 (7)
$T_0 + 4$ d	0.0 ± 0.185	0.712 ± 0.036	4.773 (7)

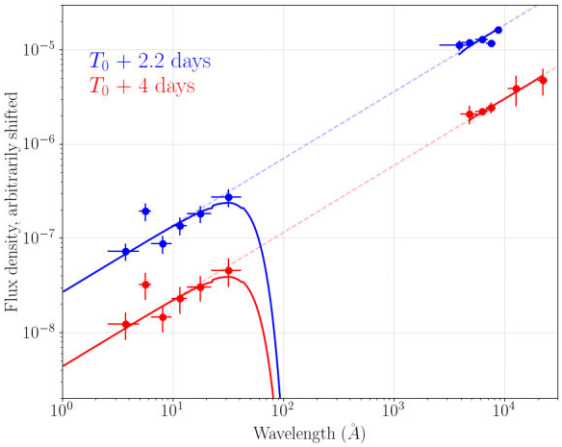

Figure 3. X-ray to NIR SED of the afterglow of GRB 230812B at $T_0 + 2.2$ d and $T_0 + 4$ d (observer-frame times). The dashed lines correspond to the best-fitting intrinsic model (single power law). The solid lines illustrate the best fit to the data, including the absorption in the X-ray. The 0.3–10 keV XRT spectrum extracted around $T_0 + 2.2$ d has been rescaled and used for the SED at $T_0 + 4$ d.

The $T_0 + 2.2$ d SED constrains best the host galaxy dust extinction as $A_V = 0.0 \pm 0.075$ mag, corresponding to a reddening of $E(B - V) = 0.0 \pm 0.026$ mag for the average SMC model with $R_V = 2.93$ (this constraint is tighter than but compatible with the upper limit $E(B - V) < 0.07$ mag (3σ) in Srinivasaragavan et al. (2024). This is consistent with the CIGALE analysis finding a very low global attenuation. We thus chose not to apply any additional extinction correction to the photometric points in Table A2.

2.3 Radio

We also added to our data set two unique submillimetre measurements from NOEMA, taken 3.8 d post T_0 : see a brief description of the analysis in de Ugarte Postigo et al. (2023b). To complete our multiwavelength data set at lower energies, we gathered the published results of radio observations of GRB230812B starting two days after T_0 and covering different radio bands from 1 to 15.5 GHz. We use the data from the Arcminute Microkelvin Imager Large-Array (Rhodes et al. 2023), the Karl G. Jansky Very Large Array (Chandra et al. 2023; Giarratana et al. 2023), and the upgraded Giant Meterwave Radio Telescope (Mohnani et al. 2023). These data are summarized in Table A1. No correction from the host constant flux and extinction were applied to these measurements.

3 SPECTRAL ANALYSIS

We performed spectroscopy of the optical counterpart of GRB 230812B on 3 epochs using OSIRIS+ (Cepa et al. 2000) on the 10.4 m Gran Telescopio Canarias (GTC) (see details in the appendix). These spectra, together with the host galaxy model derived from the SED fit are shown in Fig. 4.

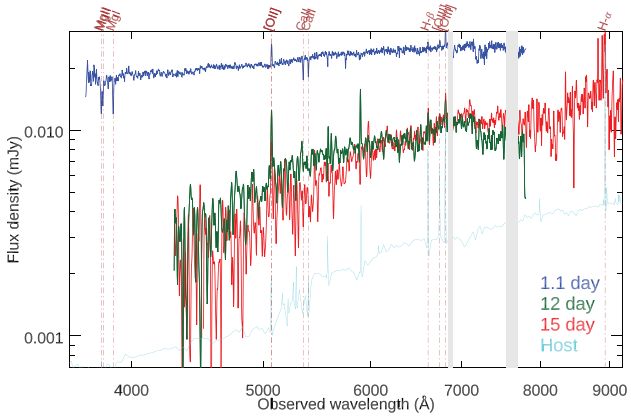

Figure 4. Spectra of GRB 230812B obtained with OSIRIS+. At 1.1 d the emission was dominated by the afterglow, with a simple power-law continuum with absorption lines from the line of sight and emission lines from the host. At 12 and 15 d the supernova component is responsible for most of the emission, with little evolution between the two epochs. We have plotted the host galaxy spectrum derived from the SED fit to understand its contribution to the observations.

Table 3. Identification and equivalent width of the spectral features observed in the afterglow spectrum.

Feature	Obs. wavelength Å	EW Å
Mg II	3801.01	2.55 ± 0.34
Mg II	3811.40	1.76 ± 0.27
MgI	3878.76	2.40 ± 0.29
[O II]/[O II]	5073.53	-2.26 ± 0.15
Ca II	5353.00	1.70 ± 0.16
Ca II	5401.00	1.52 ± 0.15
Ca I	5753.43	1.23 ± 0.15
H-beta	6614.73	-0.93 ± 0.17
[O III]	6750.73	-0.74 ± 0.16
[O III]	6813.99	-1.83 ± 0.15

The first epoch was obtained 1.1 d after the GRB, when the strong continuum was dominated by the power law, synchrotron emission of the afterglow. As already mentioned by de Ugarte Postigo et al. (2023a), the spectrum shows a strong trace with both emission and absorption lines which we identify as Mg II, Mg I, Ca II, Ca I in absorption, and [O II] and [O III] in emission, at an average redshift of 0.3602 ± 0.0006, which we identified as the refined redshift of the GRB. The spectral features and their equivalent widths (EW) are displayed in Table 3. The emission line EWs do not carry much information due to the varying continuum, but the absorption features tell us about the line of sight to the GRB within its own host galaxy. We can calculate the line strength parameter as proposed by de Ugarte Postigo et al. (2012), which determines the strength of the features as compared to a large sample of afterglows. The line of sight towards GRB 230812B displays a line strength parameter of LSP $= 0.15 \pm 0.16$, indicating that the features are just slightly stronger than the average of the sample (percentile 60 of the sample). The only significant difference with respect to the typical GRB spectrum is the relative strength of Mg I with respect to Mg II. In our case Mg I, is relatively strong, implying that the host galaxy of GRB 230812B is likely to have a low-ionized interstellar environment.

The other two epochs (12.12 and 15.12 d post T_0) show similar, broad features typical of broad-line Ic supernovae. The second epoch

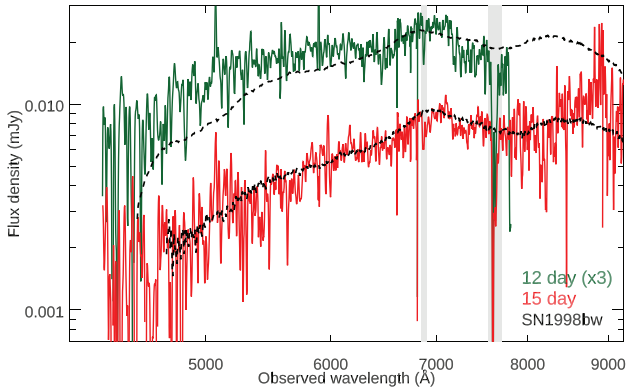

Figure 5. Comparison of the host subtracted spectra of GRB 230812B at times close to the peak of SN2023pel with spectra of SN1998bw at similar rest frame epochs.

has a slightly redder continuum, that could be due to the cooling of the ejecta. In our analysis, we consider that the contamination by the afterglow continuum is negligible at these epochs.

To analyse the clean SN spectra, we subtracted the contribution from the host galaxy using the host spectrum template that was fit to the host photometry in Section 2.2.2. The host subtracted spectra resemble well the ones obtained for SN1998bw at similar rest-frame observing epochs as was earlier noted by Agüí Fernández et al. (2023), who identify SN2023pel as a broad-line type Ic supernova.

Furthermore, we use NGSF (Goldwasser et al. 2022) on the host-subtracted spectra to determine the type of SN associated with the burst. For the spectra taken on August 27, the best matches are indeed those of type Ic, the best one being SN2006aj, at phase 2 d (after its peak), with a reduced $\chi^2/dof = 1.74$, followed by SN2002ap, SN2005ek, and SN1998bw with $\chi^2/dof = 1.77$, 1.78, and 1.79, respectively. We note that Srinivasaragavan et al. (2024) also find SN2002ap and SN1998bw to be good matches to their spectrum. See Figure 5 for a comparison of the spectra, after removing the host contribution, with SN1998bw.

Additionally, we measured the photospheric velocity of SN2023pel using host-subtracted spectra from GTC. Narrow emission lines and artefacts were first clipped using the IRAF-based routine WOMBAT, and then smoothed the spectra using the the open-source code SESNSPECTRAPCA.[15] We measure the velocity of the Fe II line near the SN peak, a proxy for the photospheric velocity of the SN, using ESNSPECTRALIB[16] (Liu et al. 2016; Modjaz et al. 2016). SESNSPECTRALIB computes the blue-shift of the Fe II 5169 Å line between a normalized SN Ic template and the pre-processed and pre-smoothed SN Ic-BL spectrum. Since the Fe II feature in a standard SN Ic spectrum is actually a combination of three lines (at 4924 Å, 5018 Å, 5169 Å), one can measure the relative blue shift of the 5169 Å line in an SN Ic-BL spectrum to a normalized SN Ic template of the same phase. The uncertainty on the velocity measurement is calculated by adding the uncertainty of the mean SN Ic template (at a particular phase) in quadrature with the uncertainty on the relative blue-shifted Fe II absorption velocity. We measure $v_{ph} = 19\,000 \pm 4000$ km s^{-1} for the spectrum taken on 2023 August 24 and $v_{ph} = 17\,000 \pm 3000$ km s^{-1} for the spectrum taken on 2023 August 27. The velocity we measure is broadly consistent with

[15] https://github.com/nyusngroup/SESNspectraPCA
[16] https://github.com/nyusngroup/SESNspectraLib

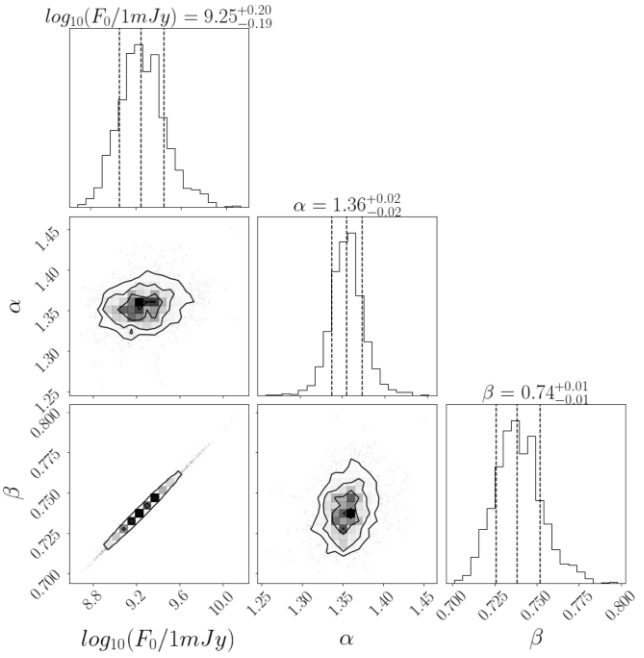

Figure 6. Posteriors of multiband fit of optical afterglow (emission up to 5 d): log of the zero-point flux (at 1 d, 1 Hz, in mJy), α the temporal decay slope and β the spectral slope.

Srinivasaragavan et al. (2024) and with that of the larger population of GRB-SNe at a similar phase Cano et al. (2017), for which the average velocity at peak is $v = 20000 \pm 8000$ km s^{-1}.

4 MULTIWAVELENGTH PHOTOMETRIC ANALYSIS OF GRB 230812B AND SN2023PEL

4.1 Empirical light-curve analysis

As a first empirical analysis of the afterglow, we perform a multiband fit of our data up to 5 d (Fig. 1, bottom), to avoid including the contribution from the emerging supernova. Assuming a power-law function of the form $F_\nu \propto t^{-\alpha} \nu^{-\beta}$, we derive a decay slope of $\alpha = 1.35 \pm 0.02$ and a spectral slope $\beta = 0.74 \pm 0.01$ (Fig. 6). We note that these values are almost identical to those obtained by Srinivasaragavan et al. (2024) for this GRB: in their work, $\alpha_o = 1.31 \pm 0.02$ and $\beta_o = 0.74 \pm 0.02$. These slopes give an indication of the physical conditions in the GRB's jet (which produces the afterglow through shocks), particularly the electron distribution's index p ($N_e(E) \propto E^{-p}$).

Using the forward shock model, different assumptions about the afterglow environment lead to different analytical equations and relations between p and α and β (Sari, Piran & Narayan 1998; Panaitescu & Kumar 2000). For instance, a fast-cooling scenario describes a spectral index $\beta = p/2$ leading to an unusual $p = 1.48 \pm 0.03$, but for a slow-cooling scenario, $\beta = (p-1)/2$, which would give a more reasonable $p = 2.48 \pm 0.03$. For the time-decay slope α, a uniform external medium gives $\alpha = (3/4)(p-1)$, which means $p = 2.80 \pm 0.04$, while a wind medium gives $\alpha = (3p-1)/4$, $p = 2.14 \pm 0.04$. The temporal and spectral indices are not satisfied by the same value of p, thus, a more sophisticated model (e.g. jet with structure) is needed, and that is what the NMMA Bayesian inference analysis will undertake.

4.2 Bayesian inference for the investigation of the jet structure, SN properties, and comparison with state of the art (using NMMA)

The GRB+SN astrophysical scenario of GRB230812B is modelled with the combination of two independent models: the semi-analytic code `afterglowpy` (van Eerten et al. 2010; Ryan et al. 2020) allowing for different structures of the jet, and the `nugent-hyper` model from `sncosmo` (Levan et al. 2005) for the supernova. We have previously used the same models on similar Kunert et al. (2024) and Kann et al. (2023)

In `afterglowpy` (van Eerten et al. 2010; Ryan et al. 2020), the thin-shell approximation is used for handling the dynamics of the relativistic ejecta propagating through the interstellar medium, and the angular structure is introduced by dissecting the blast wave into angular elements, each of which evolves independently, including lateral expansion. The analytical descriptions in Sari, Piran & Narayan (1998) are used for the magnetic-field amplification, electron acceleration, and synchrotron emission from the forward shock. The observed radiation is then computed by performing equal-time arrival surface integration. It should be noted that the model does not account for the presence of a reverse shock or an early coasting phase and does not include inverse-Compton radiation. This limits its applicability to the early afterglow of very bright GRBs. In addition, it does not allow us to explore a wind-like medium, which may be relevant in a case like GRB230812B. In `sncosmo`, the supernova modelization is constructed from observations of the supernova SN1998bw associated with the long GRB 980425.

We use the Nuclear physics and MultiMessenger Astronomy framework NMMA (Dietrich et al. 2020; Pang et al. 2023)[17] to evaluate the statistical significance of the different jet structures and provide physical properties of the GRB afterglow and the supernova component.[18] NMMA uses Bayesian inference that allows us to quantify which theoretical model $\mathcal{M}$ fits the observational data set d best by computing posterior probability distributions $\mathcal{P}(\boldsymbol{\theta}) = p(\boldsymbol{\theta}|d, \mathcal{M})$. Here $\boldsymbol{\theta}$ denotes the model's parameters. These posteriors are computed via Bayes' theorem:

$$\mathcal{P}(\boldsymbol{\theta}) = \frac{p(d|\boldsymbol{\theta}, \mathcal{M})p(\boldsymbol{\theta}|\mathcal{M})}{p(d|\mathcal{M})} = \frac{\mathcal{L}(\boldsymbol{\theta})\pi(\boldsymbol{\theta})}{\mathcal{Z}(d)}, \quad (1)$$

where $\mathcal{L}(\boldsymbol{\theta})$, $\pi(\boldsymbol{\theta})$, and $\mathcal{Z}(d)$ are called the likelihood, the prior, and the evidence, respectively. The nested sampling algorithm implemented in PYMULTINEST (Buchner 2016) is used for obtaining the posterior samples and the evidence.

Assuming a priori that the different scenarios considered are equally likely to explain the data, the plausibility of $\mathcal{M}_1$ over $\mathcal{M}_2$ is quantified by the Bayes factor

$$\mathcal{B} = \frac{p(d|\mathcal{M}_1)}{p(d|\mathcal{M}_2)}, \quad (2)$$

with $\mathcal{B} > 1 (\ln \mathcal{B} > 0)$ indicating a preference for $\mathcal{M}_1$, and vice versa. Given a set of AB magnitude measurements $\{m_i^j(t_i)\}$ (and the associated statistical uncertainties σ_i^j) across different times $\{t_i\}$ and filters $\{j\}$, the likelihood is given by

$$\mathcal{L}(\boldsymbol{\theta}) = \prod_{ij} \frac{1}{\sqrt{2\pi((\sigma_i^j)^2 + (\sigma_{\rm sys})^2)}} \exp\left(-\frac{1}{2}\frac{\left(m_i^j - m_i^{j,\rm est}(\boldsymbol{\theta})\right)^2}{(\sigma_i^j)^2 + (\sigma_{\rm sys})^2}\right) \quad (3)$$

where $m_i^{j,\rm est}(\boldsymbol{\theta})$ is the estimated AB magnitude for the parameters $\boldsymbol{\theta}$ given different models. Moreover, as an improvement over Kunert et al. (2024) and Kann et al. (2023), the systematic uncertainty $\sigma_{\rm sys}$ is treated as a free parameter and sampled over during the nested sampling and not kept fixed at a particular value. Therefore, the resulting posterior of $\sigma_{\rm sys}$ can also be interpreted as the goodness of fit. The lower the $\sigma_{\rm sys}$, the better the fit, and vice versa.

We have analysed our full data set (X-ray, UV, optical, IR, and radio)[19] with NMMA. All the values quoted in this section are medians with a 95 per cent credible interval as uncertainty.

4.2.1 *Jet structure*

We vary the jet structure of the GRB to try to characterize or to constrain the jet. To do this, we considered Gaussian (Gauss) and power-law (Power-law) jet structures. Gaussian jets feature an angular dependence $E(\theta_{\rm obs}) \propto \exp(-\theta_{\rm obs}^2/(2\theta_c^2))$ for $\theta_{\rm obs} \leq \theta_w$, with θ_w being an additional free parameter. A power-law jet features an angular dependence $E(\theta_{\rm obs}) \propto (1 + (\theta_{\rm obs}/\theta_c)^2/b)^{-b/2}$ for $\theta_{\rm obs} \leq \theta_w$, with θ_w and b being additional parameters. The resulting log Bayes factor $\ln \mathcal{B}$ of Power-law+SN relative to Tophat+SN and Gauss+SN is found to be 18.360 ± 0.020 and 17.356 ± 0.020, respectively, demonstrating a preference for the power-law jet.

The light-curve fits of our best-performing model, i.e. Power-law+SN, are shown in Fig. 7. The posterior distributions of the GRB+SN models for all jet structures considered in this work are shown in Fig. 8 (with corresponding priors displayed in Table 4). The corresponding best-fitting light curves are shown in Fig. D1 in the Appendix.

Given the Bayes factors with the interpretation of Jeffreys (1961) and Kass & Raftery (1995), one will conclude that the power-law jet is decisively favoured against the Gaussian and the top-hat jets. Yet, as previously explained, the models presented in `afterglowpy` have limitations for early-time GRB afterglow, and the early-time data are also the main source of discriminatory power between different jet structures (as seen in Fig. D1). Thus one can only conclude that there is a preference for power-law jet structure over top-hat and Gaussian jet structures, but it is not a confirmation for detecting such a structure.

In Fig. 8, we present the NMMA posteriors for the source parameters, namely the isotropic energy E_0, the interstellar medium density $n_{\rm ISM}$, the viewing angle $\theta_{\rm obs}$, the half-opening angle of the jet core $\theta_{\rm core}$, and the microphysical parameters $\{p, \epsilon_e, \epsilon_B\}$ (the power-law index of the electron energy distribution, the fraction of energy in electrons, the fraction of energy in the magnetic field, respectively) using the different jet structure models with SN.

The numerical results for the posteriors and the associated priors can be found in Table 4. For the best-fitting model, namely Power-law+SN, the posterior of p gives $p = 2.04^{+0.04}_{-0.02}$. Moreover, we find $\log_{10}(E_0/{\rm erg}) = 52.82^{+0.35}_{-0.31}$ and $\log_{10}(n_{\rm ISM}/{\rm cm}^{-3}) = -2.38^{+1.45}_{-1.60}$ which is rather low. If such an inferred low-density is not uncommon in long GRBs (GRB 990123 – Granot & Taylor 2005; GRB 090510 – Corsi, Guetta & Piro 2010; Joshi & Razzaque

[17] https://github.com/nuclear-multimessenger-astronomy/nmma

[18] In order to study and compare the statistical significance between different GRB+SN scenarios in NMMA, we assessed as a first step how statistically favoured the GRB+SN scenario (regardless of the jet structure) is compared to a compact object merger scenario. This study is presented in the Appendix D.

[19] With the exception of the K band, for which host flux contributions cannot be computed due to the absence of late-time observations.

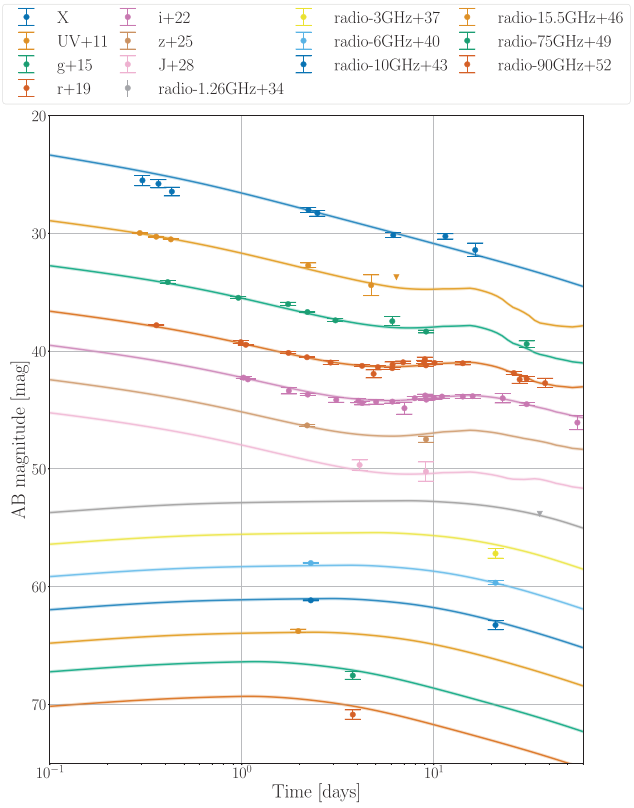

Figure 7. Best-fitting light curves of the Power-law+SN model. Datapoints are reported in the observer frame.

2021; GRB 140515A – Melandri et al. 2015; GRB 160509A – Fraija et al. 2020), it remains surprising in this case where the supernova association is strong evidence for a massive progenitor. This may reflect a strong reduction of the progenitor mass-loss in the last centuries before the collapse or that the environment had likely been blown away before the jet's interaction with it. The fractions of energy in the electrons and in the magnetic field are $\epsilon_e = 10^{-0.10^{+0.10}_{-0.29}}$ and $\epsilon_B = 10^{-2.29^{+1.02}_{-0.94}}$; and the jet's core angle $\theta_{\rm core} = 1.54^{+1.02}_{-0.81}$ deg and viewing angle $\theta_{\rm obs} = 0.76^{+1.29}_{-0.76}$ deg.

4.2.2 *Investigation on the X-ray residual*

Fig. 7 shows that the best-fitting model has substantial residuals in the X-ray band, especially at earlier times. To further understand this phenomenon, we have performed additional analyses considering data up to 5 d after trigger time, all with the power-law model, the best-performing GRB model considered. The analyses consider either only the X-ray data or only the UV, optical, and IR (UVOIR) data. The results vary in significance, as demonstrated, for instance, by the electron energy distribution index p. The analysis with the UVOIR data set gives $p = 2.39^{+0.11}_{-0.14}$, whereas the analysis with only X-ray data gives $p = 2.25^{+0.22}_{-0.27}$. We should, however, note the limitations of this restricted analysis as it results in posterior distributions that are less constrained due to the lower amount of data considered, in the X-ray band, in particular. Moreover, `afterglowpy` does not include early-time components such as a reverse shock or inverse-Compton radiation. The UVOIR data have a higher weight in the Bayesian analysis due to the higher number of data points in those bands, and since the SN model used here does not support the X-ray band, we can ascribe the high residuals in the X-ray band to a combined effect of the different sizes of the data sets in different filters and a limitation of the models considered in this work.

4.2.3 *Comparison of SN2023pel with other GRB-associated SNe*

We compare the luminosity of SN2023pel with those of several well-studied GRB-associated supernovae, namely SN1998bw, SN2006aj, and SN2013dx (Mazzali et al. 2021). To do this, we use the bolometry tool from SNooPy (Burns et al. 2011)[20] to obtain a bolometric light curve in the (450–1050) nm range. We grouped our *griz* and *J*-band data points (see Table A2) into 1-d bins. When an optical band has no observed data in a bin, we use the flux from the best-fitting model light curves as a proxy. We then subtract the bolometric flux from the GRB component of the best-fitting model from the total curve in order to get the SN component. Our results are shown in Fig. 9. We compare the maximum luminosities, the peak times, and half-max time widths of those four supernovae (SN2023pel, SN1998bw, SN2006aj, and SN2013dx, see Table 5). SN2023pel has a (rest-frame) peak time of 11.6 d, close to that of SN2013dx, but shorter than for SN1998bw and longer than for SN2006aj. It is also consistent with the average peak-time of 13.2 ± 2.6 d that Cano et al. (2017) find for a collection of GRB-SN events. However, SN2023pel notably declines somewhat faster than the other three, especially SN1998bw, with a half-max time width of 16.2 d compared to 36.0 d for the latter. We also note the differing evolution of the supernova in each band, e.g. the half-max time widths in the i' and r' bands, measured in the source frame, are $17.32^{+1.27}_{-1.23}$ d and $13.30^{+0.97}_{-0.96}$ d, respectively.

Additionally, we compute the brightness factor $k_{\rm SN}$ and (time) stretch factor $s_{\rm SN}$ (both relative to SN1998bw) to compare SN2023pel with the results of the recent Srinivasaragavan et al. (2024) paper on this supernova. We find $k_{\rm SN} = 1.08^{+0.09}_{-0.10}$ and $s_{\rm SN} = 0.67^{+0.05}_{-0.05}$, respectively. For comparison, Srinivasaragavan et al. (2024) find $k_{\rm SN} \approx 0.92$ and $s_{\rm SN} \approx 0.76$, yielding good agreement. Looking at the known correlation between brightness and time-stretch (see fig. 3 in Cano et al. 2017), SN2023pel is the brightest one among events of similar characteristic times, but still compatible with the distribution.

Further investigations have been pursued by Srinivasaragavan et al. (2024) to contextualize GRB 230812B/SN 2023pel with respect to a complete GRB-SN population beyond the three examples mentioned above [see Section 4.3 of Srinivasaragavan et al. (2024)]. Their comparison (using statistical correlations between $L_{\gamma,\ \rm iso}$ and $k_{SN,\ 1998bw}$, L_γ, iso and M_{Ni}) shows that SN 2023pel is a rather ordinary SN with respect to the overall GRB-SN population, adding more evidence that the central engine and SN powering mechanisms are decoupled in GRB-SN systems.

5 DISCUSSION AND CONCLUSION

GRB 230812B was a bright and relatively nearby gamma-ray burst that displayed a number of important features: it was accompanied by a luminous supernova, it produced radiation from a high energy of 72 GeV down to radio wavelengths, and was observed for at least a few months since the initial burst, which was detected by several space detectors. Dozens of images and measurements were taken from observatories across the world, including some 80 data points from our GRANDMA network and partner institutions, necessitating not only careful reductions and analyses but also subtractions of backgrounds, host, and Milky Way Galaxy absorption (dust) and extinction corrections, etc.

[20] https://csp.obs.carnegiescience.edu/data/snpy

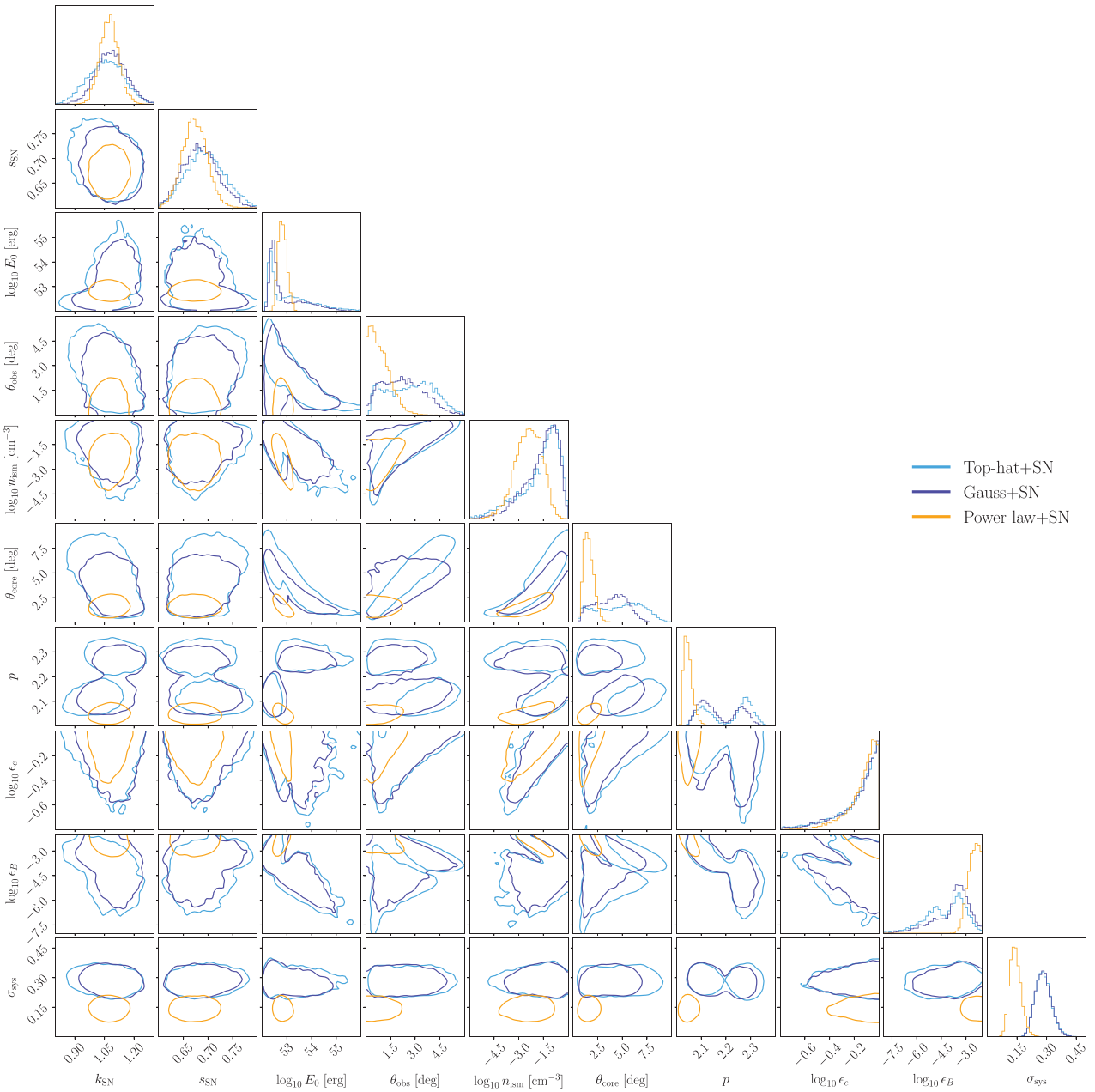

Figure 8. Posterior distribution using different jet models of `afterglowpy` and `nugent-hyper` for the supernova component.

With a duration T_{90} of 3.264 ± 0.091 s (in the [50–300] keV band), GRB 230812B falls in the 'long' category, thus (in principle) the result of a very massive star's collapse, which produces powerful jets and (oftentimes) a more isotropic supernova, which may be detected several days after the initial burst and afterglow. However, motivated by recent cases indicating that 'long' GRBs may sometimes display kilonova characteristics (which are normally associated with 'short', merger-type GRBs) and vice versa ('short' GRBs displaying collapsar-type characteristics), it was worthwhile to analyse this GRB's multiband emission to see if it is best fit with a supernova or a kilonova, in addition to determining its jet properties, i.e. geometry (observed and core angle) and physical parameters (electron and magnetic field energy fractions, etc.).

In a nutshell, our analyses (both photometric and spectral) found a clear confirmation of a supernova, and, using `NMMA`, a GRB best fit by a high (but not abnormal) total energy $E_0 = 10^{52.82^{+0.35}_{-0.31}}$ erg. The associated supernova SN2023pel peaked $15.76^{+0.81}_{-1.21}$ d (in the observer frame) after the trigger, consistent with Srinivasaragavan et al. (2024) for this supernova and similar to cases of strong GRB-SN associations (Cano et al. 2017). We also plotted pseudo-bolometric light curves for SN2023pel and three other GRB-associated supernovae (SN1998bw, SN2006aj, SN2013dx); we found this new one to have evolved similarly to the others, albeit somewhat faster (especially in decay times).

Our best-fitting model also gave a very low ambient density $n_{\rm ISM} = 10^{-2.38^{+1.45}_{-1.60}}$ cm^{-3}, similar to a number of previously modelled cases (see the brief discussion and references given above). Further investigations with different models are called for to confirm and understand all these findings.

Table 4. NMMA – Parameters and prior bounds employed in our Bayesian inferences. We report median posterior values at 95 per cent credibility for various physical scenarios and jet structures for the GRB. 'Uniform' refers to an uniform distribution, and 'LogUniform' refers to an uniform distribution for the log of the parameter. $\mathcal{N}(\mu, \sigma^2)$ refers to a Gaussian distribution with mean μ and variance σ^2.

Parameter	Prior	Prior range	Tophat+SN	Gauss+SN	Power-law+SN
(log-) Isotropic afterglow energy E_0 (erg)	Uniform	[47, 57]	$52.91^{+2.20}_{-0.78}$	$52.58^{+2.00}_{-0.42}$	$52.82^{+0.35}_{-0.31}$
(log-) Ambient medium's density $n_{\rm ism}$(cm^{-3})	Uniform	[− 6, 3]	$-1.36^{+1.34}_{-2.94}$	$-1.38^{+1.30}_{-2.27}$	$-2.38^{+1.45}_{-1.60}$
(log-) Energy fraction in electrons $\epsilon_{\rm e}$	Uniform	[− 5, 0]	$-0.13^{+0.13}_{-0.49}$	$-0.12^{+0.12}_{-0.43}$	$-0.10^{+0.10}_{-0.29}$
(log-) Energy fraction in magnetic field $\epsilon_{\rm B}$	Uniform	[− 10, 0]	$-4.02^{+1.83}_{-2.65}$	$-3.56^{+1.59}_{-2.52}$	$-2.29^{+1.02}_{-0.94}$
Electron distribution power-law index p	Uniform	[2.01, 3]	$2.25^{+0.09}_{-0.19}$	$2.15^{+0.16}_{-0.09}$	$2.04^{+0.04}_{-0.02}$
Viewing angle $\theta_{\rm obs}$ (deg)	$\mathcal{N}(0, \theta^2_{\rm core})$	–	$2.77^{+2.24}_{-2.42}$	$2.20^{+2.28}_{-2.11}$	$0.76^{+1.29}_{-0.76}$
Jet core's opening angle $\theta_{\rm core}$ (deg)	Uniform	[0.6, 18]	$4.96^{+3.30}_{-4.20}$	$3.96^{+2.45}_{-3.09}$	$1.54^{+1.02}_{-0.81}$
'Wing' truncation angle $\theta_{\rm wing}$ (deg)	Uniform	[0.6, 45]	–	$25.18^{+19.77}_{-17.50}$	$18.25^{+19.07}_{-11.48}$
Power-law structure index b	Uniform	[0.1, 7]	–	–	$1.64^{+0.49}_{-0.47}$
Angle ratio $\theta_{\rm obs}/\theta_{\rm core}$	–	–	$0.56^{+0.23}_{-0.21}$	$0.64^{+0.41}_{-0.57}$	$0.49^{+0.91}_{-0.49}$
Supernova boost $k_{\rm SN}$	Uniform	[0.01, 100]	$1.06^{+0.18}_{-0.18}$	$1.08^{+0.15}_{-0.15}$	$1.08^{+0.09}_{-0.10}$
Supernova stretch $s_{\rm SN}$	Uniform	[0.1, 5.0]	$0.69^{+0.08}_{-0.07}$	$0.68^{+0.07}_{-0.07}$	$0.67^{+0.05}_{-0.05}$
Systematic error $\sigma_{\rm sys}$	LogUniform	[0.01, 2.0]	$0.28^{+0.08}_{-0.08}$	$0.28^{+0.08}_{-0.07}$	$0.14^{+0.06}_{-0.05}$

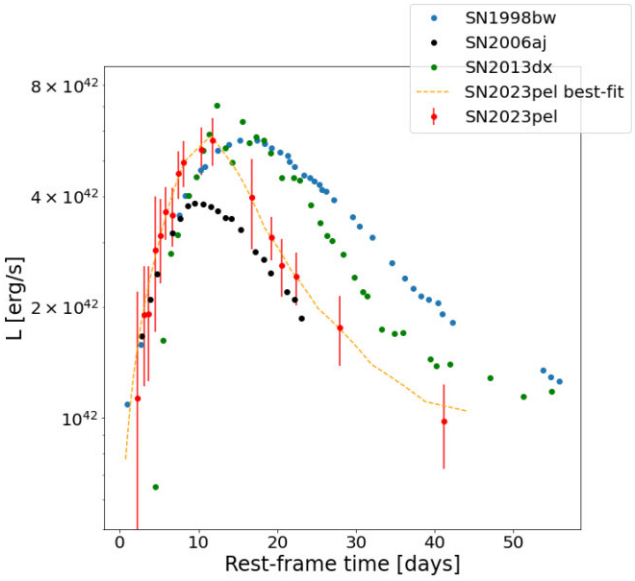

Figure 9. Comparison of pseudo-bolometric (*grizJ*) luminosity (erg s^{-1}) of SN2023pel with those of SN1998bw, SN2006aj, and SN2013dx. The dotted line shows the light curve computed from the best-fitting `nugent-hyper` model, while the points with error bars are the observational data after subtraction of the best-fitting GRB component.

Table 5. Comparison of maximum pseudo-bolometric luminosities, (rest-frame) peak times and half-max time widths of SN2023pel, SN1998bw, SN2006aj, and SN2013dx.

SN	$L_{\rm max}$ (erg s^{-1})	Peak time (d)	Half-max time width (d)
SN2023pel	5.75×10^{42}	11.6	16.2
SN1998bw	5.67×10^{42}	15.3	36.0
SN2006aj	3.80×10^{42}	9.50	26.9
SN2013dx	7.10×10^{42}	12.3	25.1

Our NMMA framework/simulation also gave best-fitting parameter values for the jet's geometry (shape and core and viewing angles) and physical conditions (electron energy distribution index, electron energy fraction, and magnetic field energy fraction). The jet's geometry/shape was best described by the (angular) 'power-law' model; the electron energy distribution index p was found to be $\approx$2.1, which is quite typical; the best-fitting magnetic field energy fraction ϵ_B was $\approx 10^{-2.4}$, also quite typical. However, the electron energy fraction was found to be rather high: $\epsilon_e \approx 0.5 - 1$ ($10^{-0.10^{+0.10}_{-0.29}}$). The jet's core and viewing angles were found to be small: $\theta_{\rm core} = 1.54^{+1.02}_{-0.81}$ deg and $\theta_{\rm obs} = 0.76^{+1.29}_{-0.76}$ deg, respectively. Despite these atypical values, the parameters still allow an on-axis jet scenario.

GRB 230812B, bright and relatively close-by, provided us (the GRANDMA network and its partners) the opportunity to perform dozens of observations in UV, optical, near infrared, and submillimetre resulting in some 80 high-quality data points. The light curves in optical showed a distinctive supernova bump, SN2023pel, which turned out to be about as bright as the famous SN1998bw. Our spectroscopic analysis determined a photospheric velocity $v_{ph} = 17\,000 \pm 3000$ km s^{-1} near the peak, and the host-subtracted spectra was best fit by SN2006aj, slightly better than SN2002ap, SN2005ek, and SN1998bw.

The rich data that we have produced, coupled with data from other groups (Srinivasaragavan et al. 2024) and facilities, will help explore this event and other GRB-SN associations with additional tools and models. Covering nine orders of magnitude in frequency, our multiband analysis presented some information about the jet and the supernova, but further investigations can help confirm or refine our results.

ACKNOWLEDGEMENTS

This work has been coordinated with Mansi Kasliwal and Brad Cenko's group, with whom we shared common developments and visions for time-domain astronomy tools and methods (e.g. SKYPORTAL). We thank Gokul Prem Srinivasaragavan in particular for fruitful exchanges on this object. We also thank the anonymous reviewer for constructive comments that have helped improve the paper.

The GRANDMA collaboration thanks its entire network of observatories/observers, all its partners in observations and analyses, and the amateur participants of its Kilonova-Catcher (KNC) programme.

We dedicate this work to D. A. Kann, whose groundbreaking work in the field of GRBs earned him international recognition over the past two decades. Alex, your contributions to the world of GRB science will always be remembered. We deeply miss you and hope you are proud of the way the GRB community carries on your legacy.

This research has also made use of the MISTRAL data base, based on observations made at Observatoire de Haute Provence (CNRS), France, with the MISTRAL spectro-imager, and operated at CeSAM (LAM), Marseille, France. The GRB OHP observing team is particularly grateful to Jérome Schmitt for the major role he has played in the development and operations of the MISTRAL instrument at the T193 telescope. GRANDMA thanks amateur astronomers for their observations: MS, KF, SL, JN, MF, MO. This work is based on observations carried out under project number S23BG with the IRAM NOEMA interferometer. Partly based on observations made with the Gran Telescopio Canarias (GTC), installed at the Spanish Observatorio del Roque de los Muchachos of the Instituto de Astrofísica de Canarias, on the island of La Palma. Partly based on observations made with the Nordic Optical Telescope, owned in collaboration by the University of Turku and Aarhus University, and operated jointly by Aarhus University, the University of Turku, and the University of Oslo, representing Denmark, Finland, and Norway, the University of Iceland and Stockholm University at the Observatorio del Roque de los Muchachos, La Palma, Spain, of the Instituto de Astrofisica de Canarias. This work is based on observations collected at the Centro Astronómico Hispano en Andalucía (CAHA) at Calar Alto, operated jointly by Junta de Andalucía and Consejo Superior de Investigaciones Científicas (IAA-CSIC) (Programme code: 23B-2.2-24, PI Agüí Fernández, J. F.). This work used Expanse at the San Diego Supercomputer Cluster through allocation AST200029 – 'Towards a complete catalog of variable sources to support efficient searches for compact binary mergers and their products' from the Advanced Cyberinfrastructure Coordination Ecosystem: Services & Support (ACCESS) programe. WC and NS wish to thank Laboratório Nacional de Astrofísica – LNA and OPD staff, Universidade do Estado do Amazonas – UEA and the Brazilian Agencies CNPq and Capes.

GRANDMA has received financial support from the CNRS through the MITI interdisciplinary programmes. TW and PTHP are supported by the research programme of the Netherlands Organization for Scientific Research (NWO). SA acknowledges the financial support of the Programme National Hautes Energies (PNHE). MWC acknowledges support from the National Science Foundation with grant numbers PHY-2347628 and OAC-2117997. CA and MWC were supported by the Preparing for Astrophysics with LSST Program, funded by the Heising-Simons Foundation through grant 2021–2975, and administered by Las Cumbres Observatory. The Egyptian team acknowledges support from the Science, Technology & Innovation Funding Authority (STDF) under grant number 45779. SK is supported by European Structural and Investment Fund and the Czech Ministry of Education, Youth and Sports (Project CoGraDS – CZ.02.1.01/0.0/0.0/15_003/0000437). NPMK is supported by the UKSA *Swift* operations grant. NG, DA, and IA acknowledge support from the American University of Sharjah (UAE) through the grant FRG22-C-S68. MM is supported by the LM2023032 and LM2023047 grants of the Ministry of Education of the Czech Republic. JM is supported by the National Key R & D Program of China (2023YFE0101200), the Yunnan Revitalization Talent Support Program (YunLing Scholar Award), and NSFC grant 12393813. DBM acknowledges support from the European Research Council (ERC) under the European Union's research and innovation programme (ERC Grant HEAVYMETAL No. 101071865). JGD is supported by a research grant from the Ile-de-France Region within the framework of the Domaine d'Intérêt Majeur-Astrophysique et Conditions d'Apparition de la Vie (DIM-ACAV). The work of FN is supported by NOIRLab, which is managed by the Association of Universities for Research in Astronomy (AURA) under a cooperative agreement with the National Science Foundation. The Kilonova-Catcher programme is supported by the IdEx Université de Paris Cité, ANR-18-IDEX-0001 and Paris-Saclay, IJCLAB. IRAM is supported by INSU/CNRS (France), MPG (Germany) and IGN (Spain). The Cosmic Dawn Center is supported by the Danish National Research Foundation. The Advanced Cyberinfrastructure Coordination Ecosystem: Services & Support (ACCESS) programe is supported by National Science Foundation grants #2138259, #2138286, #2138307, #2137603, and #2138296.

تعبّر مجموعة "جراندما" (GRANDMA) عن مواساتها وتضامنها مع سكان "أوكايمدن" عقب كارثة الزلزال الذي حدث في أغسطس 2023 بالمملكة المغربية. صادق التعازي للزملاء بمرصد "أوكايمدن" ولأهالي الضحايا، وتعاطفنا ودعمنا للمتضررين إثر هذا الحدث المفجع.

DATA AVAILABILITY

Images and raw data are available upon request.

REFERENCES

Abazajian K. N. et al., 2009, ApJS, 182, 543
Adami C. et al., 2023a, GCN Circ., 34418, 1
Adami C. et al., 2023b, GCN Circ., 34743, 1
Agüí Fernández J. F., de Ugarte Postigo A., Thoene C. C., Malesani D. B., Izzo L., Cabrera Lavers A. L., 2023, GCN Circ., 34597, 1
Agui Fernandez J. F., de Ugarte Postigo A., Thoene C. C., Malesani D. B., Izzo L., Cabrera Lavers A. L., 2023, Transient Name Server Classification Report, 2023-2115, 1
Ahumada R. et al., 2020, ApJS, 249, 3
Aivazyan V. et al., 2022, MNRAS, 515, 6007
Amram P. et al., 2023, GCN Circ., 34762, 1
Anand S. et al., 2023, preprint (arXiv:2307.11080)
Antier S. et al., 2020a, MNRAS, 492, 3904
Antier S. et al., 2020b, MNRAS, 497, 5518
Ashall C. et al., 2019, MNRAS, 487, 5824
Bellm E. C. et al., 2019, PASP, 131, 018002
Bertin E., 2010, SWarp: Resampling and Co-adding FITS Images Together, Astrophysics Source Code Library, record ascl:1010.068
Bloom J. S., Kulkarni S. R., Djorgovski S. G., 2002, AJ, 123, 1111
Boquien M., Burgarella D., Roehlly Y., Buat V., Ciesla L., Corre D., Inoue A. K., Salas H., 2019, A&A, 622, A103
Breeveld A. A., Landsman W., Holland S. T., Roming P., Kuin N. P. M., Page M. J., 2011, in McEnery J. E., Racusin J. L., Gehrels N., eds, AIP Conf. Proc. Vol. 1358, Gamma Ray Bursts 2010. Am. Inst. Phys., New York, p. 373
Buchner J., 2016, PyMultiNest: Python interface for MultiNest, Astrophysics Source Code Library, record ascl:1606.005
Bulla M., Camisasca A. E., Guidorzi C., Amati L., Rossi A., Stratta G., Singh P., 2023, GCN Circ., 33578, 1
Burns C. R. et al., 2011, AJ, 141, 19
Cano Z. et al., 2011, ApJ, 740, 41
Cano Z., Wang S.-Q., Dai Z.-G., Wu X.-F., 2017, Adv. Astron., 2017, 1
Casentini C. et al., 2023, GCN Circ., 34402, 1
Cenko B., 2023, GCN Circ., 34633, 1
Cepa J. et al., 2000, in Iye M., Moorwood A. F., eds, Proc. SPIE Conf. Ser. Vol. 4008, Optical and IR Telescope Instrumentation and Detectors. SPIE, Bellingham, p. 623

Chandra P. et al., 2023, GCN Circ., 34735, 1
Corsi A., Guetta D., Piro L., 2010, ApJ, 720, 1008
Coughlin M. W. et al., 2018, MNRAS, 478, 692
Coughlin M. W. et al., 2023, ApJS, 267, 31
D'Elia V. et al., 2015, A&A, 577, A116
de Ugarte Postigo A. et al., 2012, A&A, 548, A11
de Ugarte Postigo A., Agüí Fernández J. F., Thoene C. C., Izzo L., 2023a, GCN Circ., 34409, 1
de Ugarte Postigo A., Winters J. M., Thoene C. C., Antier S., Agüí Fernández J. F., Bremer M., Perley D. A., Martin S., 2023b, GCN Circ., 34468, 1
Deng J., Tominaga N., Mazzali P. A., Maeda K., Nomoto K., 2005, ApJ, 624, 898
Dey A. et al., 2019, AJ, 157, 168
Dietrich T., Coughlin M. W., Pang P. T. H., Bulla M., Heinzel J., Issa L., Tews I., Antier S., 2020, Science, 370, 1450
Evans P. A. et al., 2007, A&A, 469, 379
Evans P. A. et al., 2009, MNRAS, 397, 1177
Evans P. A. et al., 2010, A&A, 519, A102
Fermi GBM Team, 2023, GCN Circ., 34386, 1
Ferrero P. et al., 2006, A&A, 457, 857
Flewelling H A et al., 2020, Astrophys. J., Suppl. Ser., 25, 7
Fraija N., Laskar T., Dichiara S., Beniamini P., Duran R. B., Dainotti M., Becerra R., 2020, ApJ, 905, 112
Frederiks D., Lysenko A., Ridnaia A., Svinkin D., Tsvetkova A., Ulanov M., Cline T., Konus-Wind Team, 2023, GCN Circ., 34403, 1
Fynbo J. P. U. et al., 2006, Nature, 444, 1047
Gal-Yam A. et al., 2006, Nature, 444, 1053
Galama T. J. et al., 1998, Nature, 395, 670
Gehrels N. et al., 2004, ApJ, 611, 1005
Gehrels N. et al., 2006, Nature, 444, 1044
Gehrels N. et al., 2008, ApJ, 689, 1161
Giarratana S., Giroletti M., Ghirlanda G., Di Lalla N., Omodei N., 2023, GCN Circ., 34552, 1
Goldwasser S., Yaron O., Sass A., Irani I., Gal-Yam A., Howell D. A., 2022, Trans. Name Server AstroNote, 191, 1
Graham M. J. et al., 2019, PASP, 131, 078001
Granot J., Taylor G. B., 2005, ApJ, 625, 263
Hjorth J. et al., 2003, Nature, 423, 847
Hjorth J., Bloom J. S., 2012, in Kouveliotou C., Wijers R. A. M. J., Woosley S., eds, Chapter 9 in 'Gamma-Ray Bursts'. Cambridge Univ. Press, Cambridge, p. 169
Jeffreys H., 1961, Theory of Probability. Oxford Univ. Press, Oxford
Jin Z.-P., Li X., Cano Z., Covino S., Fan Y.-Z., Wei D.-M., 2015, ApJ, 811, L22
Jockers K. et al., 2000, Kinematika Fiz. Nebesnykh Tel Suppl., 3, 13
Joshi J. C., Razzaque S., 2021, MNRAS, 505, 1718
Kann D. A. et al., 2010, ApJ, 720, 1513
Kann D. A. et al., 2011, ApJ, 734, 96
Kann D. A. et al., 2023, ApJ, 948, L12
Karpov S., 2021, STDPipe: Simple Transient Detection Pipeline, record ascl:2112.006
Kasen D., Metzger B., Barnes J., Quataert E., Ramirez-Ruiz E., 2017, Nature, 551, 80
Kass R. E., Raftery A. E., 1995, J. Am. Stat. Assoc., 90, 773
Kuin P., Swift/UVOT Team, 2023, GCN Circ., 34399, 1
Kunert N. et al., 2024, MNRAS, 527, 3900
Lang D., Hogg D. W., Mierle K., Blanton M., Roweis S., 2010, AJ, 139, 1782
Lesage S., Burns E., Dalessi S., Roberts O., Fermi GBM Team, 2023, GCN Circ., 34387, 1
Levan A. et al., 2005, ApJ, 624, 880
Levan A. J. et al., 2023, GCN Circ., 33569, 1
Lipunov V. et al., 2023a, GCN Circ., 34389, 1
Lipunov V. et al., 2023b, GCN Circ., 34396, 1
Liu Y.-Q., Modjaz M., Bianco F. B., Graur O., 2016, ApJ, 827, 90
Malesani D. et al., 2004, ApJ, 609, L5
Mao J. et al., 2023, GCN Circ., 34404, 1
Mazzali P., Pian E., Bufano F., Ashall C., 2021, MNRAS, 505, 4106
Meegan C. et al., 2009, ApJ, 702, 791
Melandri A. et al., 2012, A&A, 547, A82
Melandri A. et al., 2015, A&A, 581, A86
Melandri A. et al., 2019, MNRAS, 490, 5366
Million C., et al. 2016 ApJ, 833, 292
Modjaz M., Liu Y. Q., Bianco F. B., Graur O., 2016, ApJ, 832, 108
Mohnani S. et al., 2023, GCN Circ., 34727, 1
Morgan J. S., Kaiser N., Moreau V., Anderson D., Burgett W., 2012, in Stepp L. M., Gilmozzi R., Hall H. J., eds, Proc. SPIE Conf. Ser. Vol. 8444, Ground-based and Airborne Telescopes IV. SPIE, Bellingham, p. 0H
Nysewander M., Fruchter A. S., Pe'er A., 2009, ApJ, 701, 824
Ochsenbein F., Bauer P., Marcout J., 2000, A&AS, 143, 23
Page K. L., Swift-XRT Team, 2023, GCN Circ., 34394, 1
Panaitescu A., Kumar P., 2000, ApJ, 543, 66
Pang P. T. H. et al., 2023, Nat. Commun., 14, 8352
Patat F. et al., 2001, ApJ, 555, 900
Pei Y. C., 1992, ApJ, 395, 130
Pian E. et al., 2006, Nature, 442, 1011
Planck Collaboration VII. 2020, A&A, 641, A7
Pyshna O. et al., 2023, GCN Circ., 34425, 1
Rastinejad J. C. et al., 2022, Nature, 612, 223
Rhodes L., Bright J., Fender R., Green D., Titterington D., 2023, GCN Circ., 34433, 1
Roberts O. J., Meegan C., Lesage S., Burns E., Dalessi S., Fermi GBM Team, 2023, GCN Circ., 34391, 1
Roming P. W. A. et al., 2005, Space Sci. Rev., 120, 95
Ryan G., van Eerten H., Piro L., Troja E., 2020, ApJ, 896, 166
Salgundi A. et al., 2023, GCN Circ., 34397, 1
Sanders N. E. et al.. 2012, The Astrophysical Journal, 756, 184
Sari R., Piran T., Narayan R., 1998, ApJ, 497, L17
Schlafly E. F., Finkbeiner D. P., 2011, ApJ, 737, 103
Schulze S. et al., 2014, A&A, 566, A102
Scotton L., Kocevski D., Racusin J., Omodei N., Fermi-LAT Collaboration, 2023, GCN Circ., 34392, 1
Soderberg A M et al. 2008, Nature, 453, 469
Srinivasaragavan G. P. et al., 2024, ApJ, 960, L18
Stanek K. Z. et al., 2003, ApJ, 591, L17
Tonry J. L. et al., 2018, PASP, 130, 064505
Troja E. et al., 2022, Nature, 612, 228
Valle M. D. et al., 2006, Nature, 444, 1050
van der Walt S. J., Crellin-Quick A., Bloom J. S., 2019, J. Open Source Softw., 4, 1247
van Eerten H., Leventis K., Meliani Z., Wijers R., Keppens R., 2010, MNRAS, 403, 300
Waters C. Z. et al., 2020, ApJS, 251, 4
Xiong S., Liu J., Huang Y., Gecam Team, 2023, GCN Circ., 34401, 1
Yang J. et al., 2022, Nature, 612, 232
Zheng W., Filippenko A. V., KAIT GRB team, 2023, GCN Circ., 34395, 1

APPENDIX A: PHOTOMETRIC OBSERVATIONS DETAILS

In this section, we detail observations for GRB 230812B by GRANDMA and associated partners. The observations of the optical afterglow of GRB 230812B started on 2023-08-13T13:34:22 UTC, 18.5 h after the trigger by the *Fermi* Gamma-ray Burst Monitor (GBM), with the GMG 2.4-m telescope, located at the Lijiang station of Yunnan Observatories. In the context of GRANDMA, this first observation was conducted after the GRANDMA collaboration decided to follow up on this GRB, which goes beyond its standard gravitational-wave follow-up programme, 12 h after the trigger time. We measured a magnitude of 19.9 ± 0.1 in the *R* band. The TAROT telescopes and other automated systems were inactive during that period.

The full observational campaign lasted 38 d and ended with observations performed by the 2-m at Observatoire de Haute Provence.

Table A1. X-ray and radio data used in this work. 'Delay' is the time interval between the start of the observation ($T_{\rm start}$) and the *Fermi* GBM's GRB trigger time (2023-08-12T18:58:12). We display both the unabsorbed flux densities and the corresponding computed AB magnitudes.

$T_{\rm start}$		Delay		Band		Flux		Instrument
UT	MJD	(d)	(s)	Central frequency	AB Magnitude	Flux density (Jy)	Error (Jy)	
				X-ray bands				
2023-08-13T02:15:22	60169.094	0.304	26230	10 keV	25.50 ± 0.45	2.29×10^{-7}	9.5×10^{-8}	*Swift* XRT
2023-08-13T03:48:00	60169.158	0.368	31788	10 keV	25.78 ± 0.35	1.77×10^{-7}	5.7×10^{-8}	*Swift* XRT
2023-08-13T05:20:10	60169.222	0.432	37317	10 keV	26.45 ± 0.37	9.55×10^{-8}	3.3×10^{-8}	*Swift* XRT
2023-08-15T00:20:43	60171.014	2.224	192151	10 keV	28.01 ± 0.25	2.27×10^{-8}	5.3×10^{-9}	*Swift* XRT
2023-08-15T06:25:05	60171.267	2.477	214012	10 keV	28.28 ± 0.26	1.77×10^{-8}	4.2×10^{-9}	*Swift* XRT
2023-08-18T22:40:51	60174.945	6.155	531759	10 keV	30.15 ± 0.20	3.15×10^{-9}	5.7×10^{-10}	*Swift* XRT
2023-08-24T07:02:27	60180.293	11.503	993854	10 keV	30.25 ± 0.23	2.89×10^{-9}	6.1×10^{-10}	*Swift* XRT
2023-08-29T05:47:45	60185.241	16.451	1421373	10 keV	31.41 ± 0.59	9.94×10^{-10}	5.4×10^{-10}	*Swift* XRT
				Radio bands				
2023-08-14T18:13:52	60170.760	1.969	170139	15.5 GHz	17.78 ± 0.16	2.8×10^{-4}	4×10^{-5}	AMI-LA
2023-08-15T01:52:24	60171.078	2.288	197652	6 GHz	18.00 ± 0.05	2.3×10^{-4}	1×10^{-5}	VLA
2023-08-15T01:52:24	60171.078	2.288	197652	10 GHz	18.17 ± 0.04	1.96×10^{-4}	7×10^{-6}	VLA
2023-08-16T13:49:00	60172.576	3.785	327048	75 GHz	18.55 ± 0.33	1.38×10^{-4}	4.2×10^{-5}	NOEMA
2023-08-16T13:49:00	60172.576	3.785	327048	90 GHz	18.87 ± 0.40	1.03×10^{-4}	3.8×10^{-5}	NOEMA
2023-09-02T18:24:52	60189.767	20.977	1812399	3 GHz	20.19 ± 0.40	3.06×10^{-5}	1.12×10^{-5}	VLA
2023-09-02T18:24:52	60189.767	20.977	1812399	6 GHz	19.67 ± 0.17	4.92×10^{-5}	7.9×10^{-6}	VLA
2023-09-02T18:24:52	60189.767	20.977	1812399	6 GHz	20.27 ± 0.39	2.82×10^{-5}	1.01×10^{-5}	VLA
2023-09-17T11:30:00	60204.479	35.689	3083508	1.26 GHz	> 19.82	$< 4.3 \times 10^{-5}$	–	uGMRT

Table A2. UVOIR observations of GRB 230812B. In column (2), $T_{(s)}$ is the time delay between the start of the observation and the *Fermi* GBM's GRB trigger time (2023-08-12T18:58:12), all in days. Column (5) gives apparent magnitudes or 5-σ upper-limits in the AB system, without any correction. Column (6) gives magnitudes in the AB systems for the afterglow and the associated SN, i.e. corrected for the host galaxy and the dust from the MW (AG + SN). When only upper limits were obtained, we corrected only for the MW dust. In Column (7), a cross means we did use this data point for the Bayesian analysis; in some cases the data were not used due to redundancy, i.e. a better measurement was made by another telescope at about the same time.

$T_{\rm start}$	$T_{\rm start}$ (d)		Filter	Exposure	Magnitude	Corrected Magnitude	Telescope	Analysis
UT	MJD	T-$T_{\rm GRB}$						
(1)	(2)		(3)	(4)	Apparent (5)	AG + SN (6)		(7)
				uv band				
2023-08-13T02:01:49	60169.085	0.294	*white*	–	19.05 ± 0.03	18.97 ± 0.03	UVOT	x
2023-08-13T03:33:56	60169.149	0.358	*white*	–	19.36 ± 0.03	19.28 ± 0.04	UVOT	x
2023-08-13T05:12:56	60169.217	0.427	*white*	–	19.58 ± 0.04	19.51 ± 0.05	UVOT	x
2023-08-15T00:12:30	60171.009	2.218	*white*	–	21.62 ± 0.11	21.72 ± 0.21	UVOT	x
2023-08-17T12:14:49	60173.510	4.720	*white*	–	22.77 ± 0.23	23.40 ± 0.88	UVOT	x
2023-08-19T04:17:04	60175.179	6.388	*white*	–	> 22.82	> 22.72	UVOT	x
				g band				
2023-08-13T04:50:07	60169.201	0.411	g'	1×300 s	19.22 ± 0.10	19.14 ± 0.10	ZTF	x
2023-08-13T18:00:11	60169.750	0.960	g'	10×180 s	20.49 ± 0.08	20.47 ± 0.08	KAO	x
2023-08-13T20:09:14	60169.840	1.049	g'	4×240 s	20.50 ± 0.03	20.48 ± 0.03	CAHA	–
2023-08-14T12:47:47	60170.533	1.743	g'	1×600 s	21.00 ± 0.14	21.01 ± 0.15	GMG	x
2023-08-14T23:41:38	60170.987	2.197	g'	1×600 s	21.6 ± 0.03	21.68 ± 0.04	NOT	x
2023-08-15T20:48:26	60171.867	3.077	g'	4×300 s	22.18 ± 0.09	22.39 ± 0.10	CAHA	x
2023-08-18 20:57:22	60174.873	6.083	g'	4×300 s	22.24 ± 0.3	22.46 ± 0.40	CAHA	x
2023-08-19T19:35:17	60175.816	7.026	g'	14×180 s	> 21.2	> 21.1	KAO	–
2023-08-21T22:00:18	60177.917	9.126	g'	3×500 s	22.83 ± 0.05	23.34 ± 0.12	NOT	x
2023-09-04T15:03:01	60191.627	22.840	g'	2×600 s	> 21.8	> 21.7	GMG	–
2023-09-12T6:38:16	60199.277	30.486	g'	10×30 s	23.32 ± 0.05	24.40 ± 0.27	CFHT-MegaCAM	x
				r band				
2023-08-13T03:34:57	60169.149	0.359	r'	1×300 s	18.85 ± 0.05	18.80 ± 0.05	ZTF	x
2023-08-13T18:41:01	60169.778	0.989	r'	10×180 s	20.19 ± 0.11	20.24 ± 0.12	KAO	x
2023-08-13T20:09:15	60169.840	1.050	r'	4x300 s	20.39 ± 0.05	20.46 ± 0.06	T193/MISTRAL	x
2023-08-13T20:23:43	60169.850	1.059	r'	4×240 s	20.38 ± 0.02	20.45 ± 0.03	CAHA	–
2023-08-14T12:58:38	60170.541	1.750	r'	1×600 s	20.98 ± 0.06	21.15 ± 0.08	GMG	x
2023-08-14T23:24:41	60170.975	2.185	r'	1×600 s	21.28 ± 0.04	21.52 ± 0.06	NOT	x
2023-08-15T16:36:09	60171.692	2.901	r'	6×100 s	21.60 ± 0.10	21.97 ± 0.15	NOWT	x
2023-08-15T21:12:19	60171.884	3.093	r'	3×300 s	21.78 ± 0.1	22.25 ± 0.17	CAHA	–
2023-08-17T00:31:21	60173.0218	4.231	r'	18×600 s	21.78 ± 0.04	22.25 ± 0.09	NOT	x
2023-08-17T15:36:49	60173.651	4.860	r'	18×200 s	22.15 ± 0.15	22.93 ± 0.34	NOWT	x
2023-08-17T21:46:15	60173.907	5.117	r'	1×1200 s	21.85 ± 0.1	22.36 ± 0.18	T193/MISTRAL	x

Table A2 – *continued*

$T_{\rm start}$ UT	$T_{\rm start}$ (d) MJD	T-$T_{\rm GRB}$	Filter	Exposure	Magnitude	Corrected Magnitude	Telescope	Analysis
(1)	(2)		(3)	(4)	Apparent (5)	AG + SN (6)		(7)
2023-08-18T20:55:50	60174.872	6.081	r'	1×600 s	21.90 ± 0.04	22.45 ± 0.10	NOT	x
2023-08-18T21:22:09	60174.890	6.100	r'	3×300 s	21.71 ± 0.14	22.14 ± 0.22	CAHA	x
2023-08-19T17:11:42	60175.716	6.926	r'	15×200 s	21.59 ± 0.07	21.95 ± 0.11	NOWT	x
2023-08-21T16:41:57	60177.696	8.905	r'	16×100 s	21.55 ± 0.07	21.90 ± 0.11	NOWT	x
2023-08-21T18:37:20	60177.776	8.986	r'	18×180 s	21.40 ± 0.13	21.69 ± 0.18	KAO	x
2023-08-21T21:32:28	60177.898	9.107	r'	1×600 s	21.76 ± 0.04	22.21 ± 0.09	NOT	x
2023-08-22T21:10:00	60178.882	10.092	r'	15×300 s	21.62 ± 0.06	22.00 ± 0.1	C2PU	x
2023-08-26T22:45:58	60182.949	14.158	r'	1×600 s	21.64 ± 0.09	22.03 ± 0.14	NOT	x
2023-09-04T15:23:48	60191.642	22.850	r'	2×600 s	> 21.7	> 21.65	GMG	–
2023-09-05T14:33:44	60192.607	23.816	r'	16×100 s	> 21.9	> 21.85	NOWT	–
2023-09-07T22:14:52	60194.927	26.136	r'	3×1800 s	22.12 ± 0.03	22.86 ± 0.13	NOT	x
2023-09-09T19:30:00	60196.813	28.022	r'	5×600 s	22.35 ± 0.10	23.41 ± 0.33	NAO-2m	x
2023-09-11T19:14:55	60198.802	30.012	r'	11×600 s	22.18 ± 0.10	23.00 ± 0.26	NAO-2m	–
2023-09-12T06:31:48	60199.272	30.482	r'	3×40 s	22.33 ± 0.05	23.36 ± 0.22	CFHT-MegaCAM	x
2023-09-12T19:30:18	60199.813	31.023	r'	11×600 s	22.31 ± 0.10	23.31 ± 0.31	NAO-2m	
2023-09-19T19:58:00	60206.832	38.042	r'	9×600 s	22.45 ± 0.1	23.72 ± 0.41	T193/MISTRAL	x
				i band				
2023-08-13T19:28:23	60169.811	1.021	i'	2×150 s	20.16 ± 0.05	20.25 ± 0.06	KAO	x
2023-08-13T20:46:19	60169.865	1.705	i'	3×240 s	20.29 ± 0.03	20.40 ± 0.04	CAHA	x
2023-08-14T13:09:36	60170.548	1.758	i'	1×600 s	21.08 ± 0.20	21.37 ± 0.27	GMG	x
2023-08-14T23:52:51	60170.995	2.205	i'	1×300 s	21.31 ± 0.06	21.69 ± 0.11	NOT	x
2023-08-15T21:30:45	60171.896	3.106	i'	4×300 s	21.59 ± 0.11	22.14 ± 0.21	CAHA	x
2023-08-16T20:12:30	60172.842	4.052	i'	9×300 s	21.64 ± 0.07	22.22 ± 0.16	NAO-2m	x
2023-08-17T00:42:36	60173.030	4.239	i'	1×600s	21.74 ± 0.06	22.41 ± 0.16	NOT	x
2023-08-17T19:12:05	60173.800	5.001	i'	14×300s	21.69 ± 0.09	22.31 ± 0.19	NAO-2m	x
2023-08-18T21:07:04	60174.880	6.089	i'	1×600 s	21.68 ± 0.04	22.29 ± 0.12	NOT	x
2023-08-18T21:39:40	60174.903	6.112	i'	4×300 s	21.64 ± 0.15	22.22 ± 0.19	CAHA	–
2023-08-19T19:50:40	60175.827	7.037	i'	20×180 s	21.95 ± 0.20	22.85 ± 0.51	KAO	x
2023-08-20T18:01:44	60176.751	7.961	i'	29×180 s	21.51 ± 0.06	22.00 ± 0.12	KAO	x
2023-08-21T19:41:01	60177.820	9.030	i'	20×180 s	21.36 ± 0.06	21.77 ± 0.11	KAO	x
2023-08-21T22:27:57	60177.936	9.146	i'	1×600 s	21.58 ± 0.04	22.12 ± 0.11	NOT	x
2023-08-22T19:30:17	60178.813	10.022	i'	20×180 s	21.49 ± 0.09	21.97 ± 0.16	KAO	x
2023-08-23T19:56:13	60179.831	11.040	i'	19×180 s	21.42 ± 0.07	21.86 ± 0.13	KAO	x
2023-08-26T22:57:10	60182.956	14.165	i'	1×600 s	21.42 ± 0.08	21.86 ± 0.14	NOT	x
2023-08-28T19:20:25	60184.806	16.015	i'	26×180 s	21.40 ± 0.11	21.83 ± 0.18	KAO	x
2023-09-04T15:50:00	60191.660	22.870	i'	2×600 s	21.51 ± 0.24	22.00 ± 0.40	GMG	x
2023-09-12T06:24:15	60199.267	30.476	i'	3×60 s	21.79 ± 0.04	22.51 ± 0.14	CFHT-MegaCAM	x
2023-10-07T19:44:24	60224.822	56.032	i'	1×3000 s	22.34 ± 0.04	24.07 ± 0.60	NOT	–
				z band				
2023-08-14T13:20:38	60170.556	1.766	z'	1×600 s	> 20.5	> 20.47	GMG	–
2023-08-14T23:30:23	60170.979	2.189	z'	1×600 s	20.98 ± 0.08	21.31 ± 0.12	NOT	x
2023-08-21T21:43:40	60177.905	9.115	z'	1×900 s	21.68 ± 0.10	22.49 ± 0.26	NOT	x
				J band				
2023-08-16T21:33:58	60172.899	4.108	J	20×50 s	21.00 ± 0.17	21.67 ± 0.43	TNG	–
2023-08-21T21:29:22	60177.895	9.105	J	45×60 s	21.26 ± 0.27	22.23 ± 0.57	TNG	–
2023-10-11T20:15:22	60228.844	60.054	J	45×80 s	21.82 ± 0.32	–	TNG	–
				K band				
2023-08-16T20:49:28	60172.868	4.077	K	30×50 s	21.41 ± 0.33	21.40 ± 0.33 with host	TNG	–

While we took images in V, R, I, g', r', i', and z' bands, we use for this work only data in g', r', i', and z' bands for extracting the physical properties of the event. We however computed the synthetic light curves in R, I from the `NMMA` best-fitting parameters constrained from the Xray+UV+*griz*+radio analysis, and confirmed their consistency with our data sets.

Below, in sequence, we here provide the start time (relative to T_0) of the first observation for each telescope and the filters/bands used during the entire campaign: GMG (0.78 d in R, g', r', i', z') at Lijiang station of Yunnan Observatories, UBAI-AZT-22 (0.91 d in R band) at Maidanak Observatory, AC-32 telescope at Abastumani observatory (0.94 d in R), KAO (0.96 d in g', r', i') at Kottamia Observatory, Lisnyky-Schmidt (0.98 d in R) at Kyiv Observatory, NAO-50/70 cm Schmidt (1.03 d in I) at Rozhen National Astronomical Observatory, CAHA (1.049 d in g', r', i') at Calar Alto Astronomical Observatory, T193/MISTRAL (1.050 d in r') at Haute-Provence Observatory, the 2-m telescope (1.08 d in R) at Shamakhy Astrophysical Observatory of Azerbaijan, FRAM-CTA-N (1.12 d in R) at Roque de los Muchachos Observatory, NOWT (2.09 d in BVR) at Xinjiang Astronomical Observatory, NOT (2.185 d in g', r', i') at Roque de los Muchachos

Observatory, NAO-2 m (4.05 d in r', i') at Rozhen NAO,[21] C2PU (10.10 d in r') at Calern observatory, CFHT-Megacam (30.48 d in g', r', i') at Mauna Kea Observatory.

Near-infrared (NIR) observations of GRB 230812B were carried out with the Italian 3.6-m TNG telescope, sited in Canary Island, using the NICS instrument in imaging mode. A series of images were obtained with the J and K filters on 2023 August 16 (i.e. about 4.1 d after the burst) and with the J filter only on 2023 August 21 and 2023 October 11 (i.e. about 9.1 and 60.1 d after the burst).

In addition to the professional network, GRANDMA activated its Kilonova-Catcher (KNC) citizen science programme for further observations with amateurs' telescopes.

The GRANDMA observations and its partners are listed in Table A2, which includes the start time $T_{\rm mid}$ time (in ISO format with post-trigger delay) and the host-galaxy/extinction-corrected brightness (in AB magnitudes) of the observations, as well as the uncorrected magnitudes. The exposure times, names of telescopes, and filters used are mentioned for each observation. Our method for calculating the magnitudes is described in the Section 2.2, including our methods of photometry transient detection, magnitude system conversion, Milky Way extinction correction, and host galaxy flux subtraction.

APPENDIX B: SPECTROSCOPIC OBSERVATION DETAILS

We used OSIRIS+ (Cepa et al. 2000) mounted on the 10.4m Gran Telescopio Canarias (GTC) telescope at Roque de los Muchachos Observatory in La Palma, Canary Islands, Spain, to observe the afterglow and supernova that follow GRB 230812B. The observation consisted of spectroscopy with an exposure time of 3x900s and grism R1000B, with a wavelength coverage between 3600 and 7800 AA. The first spectrum started at 21:37 UT, 1.110 d after the burst, while the on 2023 August 24 at 21.79 h UT, 12.12 d after the GRB detection, close to the peak of the supernova emission (Agüí Fernández et al. 2023; de Ugarte Postigo et al. 2023a).

The last two epochs were initially programmed to be obtained with larger spacing between epochs, but due to weather and telescope scheduling they ended up being rather close in time. The first epoch was obtained with a single grism, R1000B, covering the range between 3700 and 7880 Å. The second epoch included two grisms, R1000B and R1000R, this second one adding coverage between 5100 and 10100 Å to cover the full optical spectrum.

APPENDIX C: SKYPORTAL

To store, display, and annotate GRANDMA data products in a follow-up campaign, we use SKYPORTAL (van der Walt, Crellin-Quick & Bloom 2019; Coughlin et al. 2023), a powerful data base, API, and web application for time-domain astronomy. We use it for its capabilities of ingesting multimessenger triggers from GCNs in real-time, from where network-cognizant observation plans are automatically generated using GWEMOPT (Coughlin et al. 2018). It also enables automated ingestion of transients from the Transient Name Server (TNS) identified by surveys such as the Zwicky Transient Facility (Bellm et al. 2019; Graham et al. 2019), the Panoramic Survey Telescope and Rapid Response System (Pan-STARRS) (Morgan et al. 2012), or the Asteroid Terrestrial-impact Last Alert System (ATLAS) (Tonry et al. 2018); it is from TNS that we retrieved the discovery photometry. We store photometry information, including flux and limiting magnitude measurements from follow-up observations by GRANDMA's telescopes within SKYPORTAL, supplementing the data imported from TNS, to create light curves. From the dedicated source page, easy access is provided to many other data base services, such as Vizier (Ochsenbein, Bauer & Marcout 2000). Finally, SKYPORTAL is used for simplifying interactions with Bayesian inference frameworks such as the Nuclear physics and Multimessenger Astronomy framework NMMA (Dietrich et al. 2020; Pang et al.), which we discuss more in the main text. Operations on SKYPORTAL are conducted and monitored by 'shifters', members of the collaboration organized in teams every week, and divided into four daily slots of six hours each to accommodate timezone constraints while maintaining 24/7 coverage. Shifters look out for new candidates from surveys (particularly LIGO-Virgo-KAGRA, LVK) and new GCN events on the platform and report on associated Slack channels which candidates are to be followed up or not based on pre-defined criteria. The shifts are also organized using SKYPORTAL's dedicated page in the form of a calendar. Shifters or members of telescope teams are expected to upload executed observations data either manually or programmatically using the API. GCN circular-like documents can even be automatically generated, ensuring consistent formatting of the results reported to the General Coordinates Network while reducing the possibility for human errors to be made.

APPENDIX D: COMPARING DIFFERENT ASTROPHYSICAL SCENARIOS WITH NMMA

As discussed in Section 4.2, using NMMA, we can quantitatively compare different astrophysical scenarios in a Bayesian framework. We have performed studies using various models and jet geometries. NMMA is able to perform joint Bayesian inference of multimessenger events containing gravitational waves, GRB afterglows, SNe, or kilonovae. In addition to scenarios mentioned above, we also consider two kilonova models, Bu2023Ye (Anand et al. 2023) and Ka2017 (Kasen et al. 2017), to accompany the Top-hat model as possible explanations of the data set. The log Bayes factor $\ln \mathcal{B}$ of various models relative to the Power-law+SN, which is the best-performing model to be introduced shortly, can be found in Table D1. The posterior of $\sigma_{\rm sys}$ is also shown in Table D1. The Power-law+SN has the lowest value of $\sigma_{\rm sys}$, thus signifying a better fit compared to other models. Comparing the differences between the log Bayes factor of scenarios with and without an SN component, we conclude that the presence of an SN component is statistically supported from a Bayesian perspective.

The posterior values of all the considered models is summarized in Table D2. The best-fitting light curves for the three GRB+SN scenarios are shown in Fig. D1.

[21] Using the focal reducer FoReRo-2 (Jockers et al. 2000).

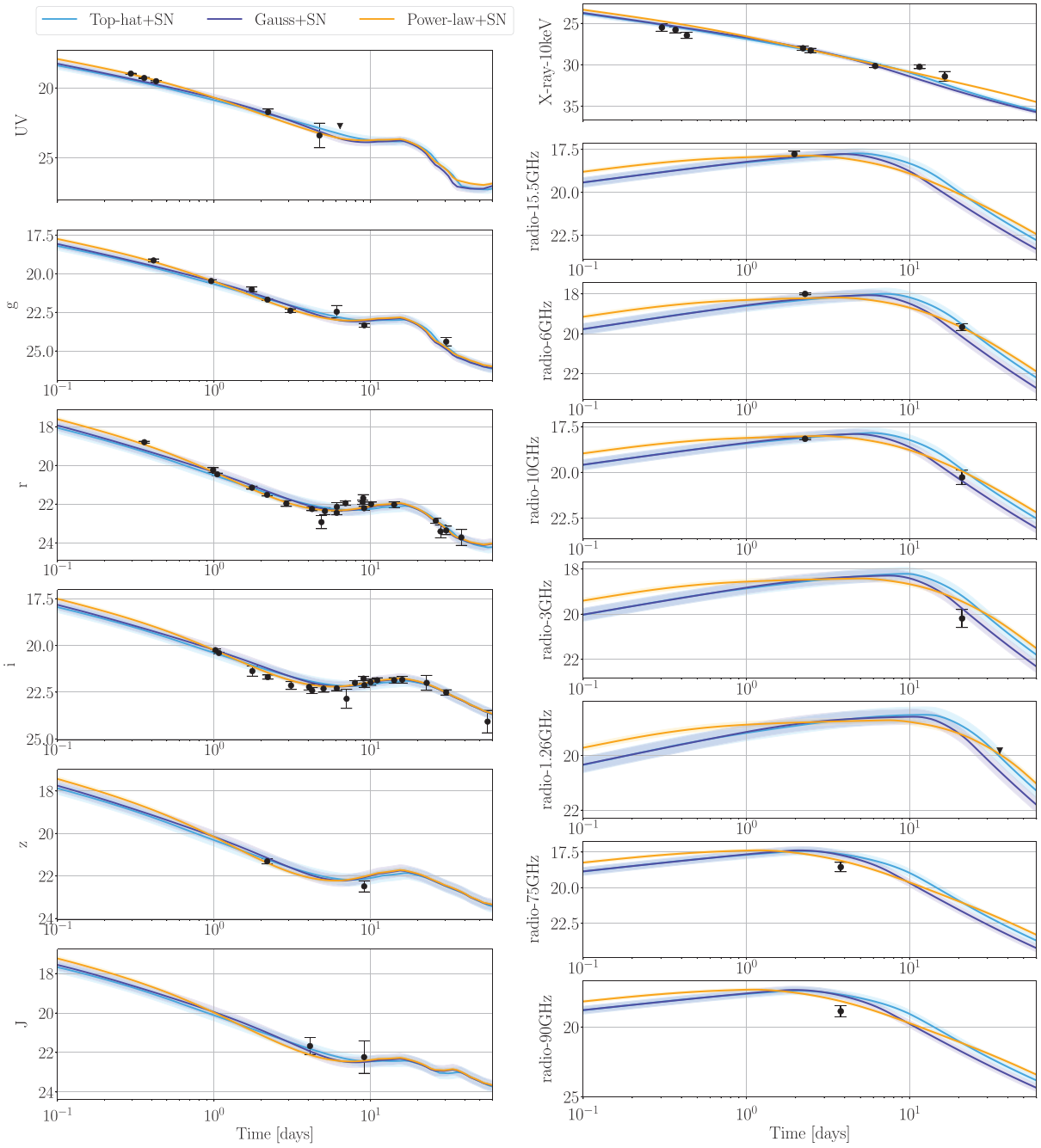

Figure D1. Best-fitting light curves of the GRB+SN models with top-hat, Gaussian, and power-law jet structures. Datapoints are reported in the observer frame.

Table D1. The log Bayes factor $\ln \mathcal{B}$ and $\sigma_{\rm sys}$ value (median with 95 per cent credible interval) inferred for different models.

Scenario	log Bayes factor $\ln \mathcal{B}$	$\sigma_{\rm sys}$ (mag)
Power-law+SN	ref	$0.140^{+0.061}_{-0.050}$
Top-hat	-56.612 ± 0.298	$0.693^{+0.133}_{-0.117}$
Top-hat+SN	-18.360 ± 0.331	$0.282^{+0.081}_{-0.077}$
Top-hat+Bu2023Ye	-56.682 ± 0.297	$0.696^{+0.126}_{-0.103}$
Top-hat+Ka2017	-56.633 ± 0.297	$0.696^{+0.125}_{-0.108}$
Gauss	-56.235 ± 0.298	$0.690^{+0.122}_{-0.116}$
Gauss+SN	-17.356 ± 0.331	$0.282^{+0.080}_{-0.073}$
Power-law	-56.292 ± 0.296	$0.693^{+0.127}_{-0.111}$

Table D2. NMMA – Parameters and prior bounds employed in our Bayesian inferences. We report median posterior values at 95 per cent credibility for various physical scenarios and jet structures for the GRB. 'Uniform' refers to an uniform distribution, and 'LogUniform' refers to an uniform distribution for the log of the parameter. $\mathcal{N}(\mu, \sigma^2)$ refers to a Gaussian distribution with mean μ and variance σ^2.

			Top-hat						
Parameter	Prior	Prior range		+SN	+Bu2023Ye	+Ka2017	Gauss	Gauss+SN	Power-law	Power-law+SN
(log-) Isotropic afterglow energy E_0 (erg)	Uniform	[47, 57]	$52.39^{+0.40}_{-0.44}$	$52.91^{+2.20}_{-0.78}$	$52.37^{+0.38}_{-0.41}$	$52.39^{+0.43}_{-0.39}$	$52.60^{+0.68}_{-0.53}$	$52.58^{+2.00}_{-0.42}$	$52.48^{+0.45}_{-0.47}$	$52.82^{+0.35}_{-0.31}$
(log-) Ambient medium's density $n_{\rm ism}(\rm cm^{-3})$	Uniform	[− 6, 3]	$-4.76^{+1.36}_{-1.23}$	$-1.36^{+1.34}_{-2.94}$	$-4.84^{+1.21}_{-1.13}$	$-4.89^{+1.34}_{-1.10}$	$-4.63^{+1.65}_{-1.30}$	$-1.38^{+1.30}_{-2.27}$	$-4.80^{+1.37}_{-1.17}$	$-2.38^{+1.45}_{-1.60}$
(log-) Energy fraction in electrons $\epsilon_{\rm e}$	Uniform	[− 5, 0]	$-0.48^{+0.39}_{-0.38}$	$-0.13^{+0.13}_{-0.49}$	$-0.53^{+0.39}_{-0.33}$	$-0.56^{+0.39}_{-0.33}$	$-0.48^{+0.42}_{-0.36}$	$-0.12^{+0.12}_{-0.43}$	$-0.50^{+0.40}_{-0.35}$	$-0.10^{+0.10}_{-0.29}$
(log-) Energy fraction in magnetic field $\epsilon_{\rm B}$	Uniform	[− 10, 0]	$-0.55^{+0.47}_{-0.86}$	$-4.02^{+1.83}_{-2.65}$	$-0.52^{+0.45}_{-0.75}$	$-0.52^{+0.44}_{-0.80}$	$-0.65^{+0.56}_{-1.02}$	$-3.56^{+1.59}_{-2.52}$	$-0.52^{+0.44}_{-0.83}$	$-2.29^{+1.02}_{-0.94}$
Electron distribution power-law index p	Uniform	[2.01, 3]	$2.13^{+0.13}_{-0.08}$	$2.25^{+0.09}_{-0.19}$	$2.14^{+0.11}_{-0.09}$	$2.15^{+0.11}_{-0.09}$	$2.13^{+0.13}_{-0.08}$	$2.15^{+0.16}_{-0.09}$	$2.13^{+0.12}_{-0.08}$	$2.04^{+0.04}_{-0.02}$
Viewing angle $\theta_{\rm obs}$ (deg)	$\mathcal{N}(0, \theta^2_{\rm core})$	–	$4.26^{+9.18}_{-4.26}$	$2.77^{+2.24}_{-2.42}$	$3.28^{+6.28}_{-3.28}$	$3.59^{+6.36}_{-3.58}$	$8.62^{+11.51}_{-8.61}$	$2.20^{+2.28}_{-2.11}$	$7.33^{+11.16}_{-7.33}$	$0.76^{+1.29}_{-0.76}$
Jet core's opening angle $\theta_{\rm core}$ (deg)	Uniform	[0.6, 18]	$13.25^{+4.74}_{-6.35}$	$4.96^{+3.30}_{-4.20}$	$13.20^{+4.80}_{-5.75}$	$13.38^{+4.61}_{-5.55}$	$11.02^{+6.98}_{-7.25}$	$3.96^{+2.45}_{-3.09}$	$12.01^{+5.98}_{-6.89}$	$1.54^{+1.02}_{-0.81}$
'Wing' truncation angle $\theta_{\rm wing}$ (deg)	Uniform	[0.6, 45]	–	–	$22.28^{+21.71}_{-19.59}$	$21.97^{+20.71}_{-20.47}$	$27.83^{+17.10}_{-16.05}$	$25.18^{+19.77}_{-17.50}$	$29.21^{+15.62}_{-16.96}$	$18.25^{+19.07}_{-11.48}$
Power-law structure index b	Uniform	[0.1, 7]	–	–	$3.48^{+3.03}_{-3.36}$	$3.46^{+3.07}_{-3.36}$	–	–	$3.46^{+3.16}_{-3.27}$	$1.64^{+0.49}_{-0.47}$
Angle ratio $\theta_{\rm obs}/\theta_{\rm core}$	–	–	$0.33^{+0.64}_{-0.32}$	$0.56^{+0.23}_{-0.21}$	$0.27^{+0.36}_{-0.27}$	$0.29^{+0.37}_{-0.29}$	$1.03^{+0.87}_{-1.03}$	$0.64^{+0.41}_{-0.57}$	$0.68^{+0.97}_{-0.68}$	$0.49^{+0.91}_{-0.49}$
Supernova boost $k_{\rm SN}$	Uniform	[0.01, 100]	–	$1.06^{+0.18}_{-0.18}$	–	–	–	$1.08^{+0.15}_{-0.15}$	–	$1.08^{+0.09}_{-0.10}$
Supernova stretch $s_{\rm SN}$	Uniform	[0.1, 5.0]	–	$0.69^{+0.08}_{-0.07}$	–	–	–	$0.68^{+0.07}_{-0.07}$	–	$0.67^{+0.05}_{-0.05}$
Systematic error $\sigma_{\rm sys}$	LogUniform	[0.01, 2.0]	$0.69^{+0.13}_{-0.12}$	$0.28^{+0.08}_{-0.08}$	$0.70^{+0.13}_{-0.10}$	$0.70^{+0.12}_{-0.11}$	$0.69^{+0.12}_{-0.12}$	$0.28^{+0.08}_{-0.07}$	$0.69^{+0.13}_{-0.11}$	$0.14^{+0.06}_{-0.05}$

[1]*IJCLab, Univ Paris-Saclay, CNRS/IN2P3 Orsay, 91405, France*
[2]*Nikhef, Science Park 105, NL-1098 XG Amsterdam, the Netherlands*
[3]*Institute for Gravitational and Subatomic Physics (GRASP), Utrecht University, Princetonplein 1, NL-3584 CC Utrecht, the Netherlands*
[4]*Physics Department, American University of Sharjah, Sharjah, 26666, UAE*
[5]*National Research Institute of Astronomy and Geophysics (NRIAG), 1 Elmarsad St., 11421 Helwan, Cairo, Egypt*
[6]*Aix Marseille Univ, CNRS, CNES, 13388 LAM Marseille, France*
[7]*Instituto de Astrofísica de Andalucía, Glorieta de la Astronomía s/n, E-18008 Granada, Spain*
[8]*Cahill Center for Astrophysics, California Institute of Technology, Pasadena, CA 91125, USA*
[9]*E. Kharadze Georgian National Astrophysical Observatory, Mt. Kanobili, Abastumani 0301, Adigeni, Georgia*
[10]*Samtskhe-Javakheti State University, Rustaveli Str. 113, Akhaltsikhe 0080, Georgia*
[11]*School of Physics and Astronomy, University of Minnesota, Minneapolis, MN 55455, USA*
[12]*Observatoire de la Côte d'Azur, Université Côte d'Azur, Boulevard de l'Observatoire, F-06304 Nice, France*
[13]*INAF–Osservatorio Astronomico di Brera, Via E. Bianchi 46, I-23807 Merate (LC), Italy*
[14]*Astronomical Observatory of Taras Shevchenko National University of Kyiv, Observatorna Str. 3, UA-04053 Kyiv, Ukraine*
[15]*CEICO, Institute of Physics of the Czech Academy of Sciences, Na Slovance 1999/2, CZ-182 21 Praha, Czech Republic*
[16]*Centro Astronómico Hispano en Andalucía, Observatorio de Calar Alto, Sierra de los Filabres, E-04550 Gérgal, Almería, Spain*
[17]*Laboratoire J.-L. Lagrange, Université de Nice Sophia-Antipolis, CNRS, Observatoire de la Côte d'Azur, F-06304 Nice, France*
[18]*National Observatory of Athens, Institute for Astronomy, Astrophysics, Space Applications and Remote Sensing, GR-15236 Penteli, Greece*
[19]*Institut de Radioastronomie Millimétrique, Saint-Martin-d'Hères, 38406, France,*
[20]*Università degli Studi dell'Insubria, Dipartimento di Scienza e Alta Tecnologia, Via Valleggio 11, I-22100 Como, Italy*
[21]*Department of Physics and Earth Science, University of Ferrara, via Saragat 1, I-44122 Ferrara, Italy*
[22]*INFN, Sezione di Ferrara, via Saragat 1, I-44122 Ferrara, Italy*
[23]*INAF, Osservatorio Astronomico d'Abruzzo, via Mentore Maggini snc, I-64100 Teramo, Italy*
[24]*Ulugh Beg Astronomical Institute, Uzbekistan Academy of Sciences, Astronomy Str. 33, Tashkent 100052, Uzbekistan*
[25]*Department of Physics and Astronomy, Louisiana State University, Baton Rouge, LA 70803, USA*
[26]*Astrophysics Science Division, NASA Goddard Space Flight Center, 8800 Greenbelt Rd, Greenbelt, MD 20771, USA*
[27]*Joint Space-Science Institute, University of Maryland, College Park, MD 20742, USA*
[28]*Laboratório Nacional de Astrofísica - LNA, Rua Estados Unidos, 154 Itajubá - MG CEP 37504-364, Brazil*
[29]*Sorbonne Université, CNRS, UMR 7095, Institut d'Astrophysique de Paris, 98 bis bd Arago, F-75014 Paris, France*
[30]*Institute for Physics and Astronomy, University of Potsdam, Haus 28, Karl-Liebknecht-Str. 24/25, D-14476 Potsdam, Germany*
[31]*Max Planck Institute for Gravitational Physics (Albert Einstein Institute), Am Mühlenberg 1, D-14476 Potsdam, Germany*
[32]*Aix Marseille Univ, CNRS/IN2P3, CPPM, 13288 Marseille, France*
[33]*Université Paris Cité, CNRS, Astroparticule et Cosmologie, F-75013 Paris, France*
[34]*Université Paris-Saclay, Université Paris Cité, CEA, CNRS, AIM, F-91191 Gif-sur-Yvette, France*
[35]*KNC, AAVSO, Hidden Valley Observatory (HVO), Colfax, WI, 54730, USA; iTelescope, New Mexico Skies Observatory, Mayhill, NM, 88339, USA*
[36]*Cosmic Dawn Center (DAWN), 2200 Copenhagen, Denmark*
[37]*Niels Bohr Institute, University of Copenhagen, Jagtvej 128, DK-2200 Copenhagen N, Denmark*

[38]*N. Tusi Shamakhy Astrophysical Observatory, Ministry of Science and Education, settl. Y. Mammadaliyev, AZ-5626 Shamakhy, Azerbaijan*
[39]*School of Physics and Astronomy, University of Minnesota, Minneapolis, MN 55455, USA*
[40]*Xinjiang Astronomical Observatory (XAO), Chinese Academy of Sciences, Urumqi 830011, P. R. China*
[41]*INAF–Osservatorio Astronomico di Capodimonte, Salita Moiariello 16, I-80131 Napoli, Italy*
[42]*DARK, Niels Bohr Institute, University of Copenhagen, Jagtvej 128, DK-2200 Copenhagen N, Denmark*
[43]*Division of Physics, Mathematics, and Astronomy, California Institute of Technology, Pasadena, CA 91125, USA*
[44]*IRAP, Université de Toulouse, CNRS, UPS, 14 Avenue Edouard Belin, F-31400 Toulouse, France*
[45]*Université Paul Sabatier Toulouse III, Université de Toulouse, 118 Route de Narbonne, F-31400 Toulouse, France*
[46]*Mullard Space Science Laboratory, University College London, Holmbury St. Mary Dorking RH5 6NT, UK*
[47]*Montarrenti Observatory, S. S. 73 Ponente, I-53018 Sovicille, Siena, Italy*
[48]*Yunnan Observatories, Chinese Academy of Sciences, 650011 Kunming, Yunnan Province, P. R. China*
[49]*Department of Astrophysics/IMAPP, Radboud University, NL-6525 AJ Nijmegen, the Netherlands*
[50]*FZU–Institute of Physics of the Czech Academy of Sciences, Na Slovance 1999/2, CZ-182 21 Praha, Czech Republic*
[51]*Center for Astronomical Mega-Science, Chinese Academy of Sciences, 20A Datun Road, Chaoyang District, 100012 Beijing, P. R. China*
[52]*Key Laboratory for the Structure and Evolution of Celestial Objects, Chinese Academy of Sciences, 650011 Kunming, P. R. China*
[53]*INAF–Osservatorio Astronomico di Roma, Via di Frascati 33, I-00040 Monte Porzio Catone (RM), Italy*
[54]*Institute of Astronomy and NAO, Bulgarian Academy of Sciences, 72 Tsarigradsko Chaussee Blvd., 1784 Sofia, Bulgaria*
[55]*SOAR Telescope/NSF's NOIRLab Avda Juan Cisternas 1500, 1700000 La Serena, Chile*
[56]*GEPI, Observatoire de Paris, Université PSL, CNRS, 5 place Jules Janssen, F-92190 Meudon, France*
[57]*Mathematics, Informatics, Physics and Earth Science Department, University of Messina, Via F.D. D'Alcontres 31, Polo Papardo, I-98166 Messina, Italy*
[58]*Physics Department, Tsinghua University, Beijing 100084, P. R. China*
[59]*Université de Strasbourg, CNRS, IPHC UMR 7178, F-67000 Strasbourg, France*
[60]*Kavli Institute for Astrophysics and Space Research, Massachusetts Institute of Technology, 77 Massachusetts Ave, Cambridge, MA 02139, USA*
[61]*Société Astronomique de France, Observatoire de Dauban, F-04150 Banon, France*
[62]*Astronomy and Space Physics Department, Taras Shevchenko National University of Kyiv, Glushkova Ave., 4, UA-03022 Kyiv, Ukraine*
[63]*National Center Junior Academy of Sciences of Ukraine, Dehtiarivska St. 38-44, UA-04119 Kyiv, Ukraine*
[64]*Main Astronomical Observatory of National Academy of Sciences of Ukraine, 27 Acad. Zabolotnoho Str., UA-03143 Kyiv, Ukraine*
[65]*Department of Astronomy, University of Maryland, College Park, MD 20742, USA*
[66]*Department of Physics, Eastern Illinois University, Charleston, IL 61920, USA*
[67]*Department of Physics and Astronomy, University of Leicester, University Road, Leicester LE1 7RH, UK*
[68]*Astronomical Institute of the Czech Academy of Sciences (ASU-CAS), Fricova 298, CZ-251 65 Ondřejov, Czech Republic*
[69]*National University of Uzbekistan, Department of Astronomy and Atmospheric Physics, 4 University Str., Tashkent 100174, Uzbekistan*
[70]*Department of Physics and Astronomy, University of Catania, Via Santa Sofia 64, I-95123 Catania, Italy*
[71]*Beijing Planetarium, Beijing Academy of Science and Technology, Beijing 100044, P. R. China*
[72]*Department of Astronomy, School of Physics, Huazhong University of Science and Technology, Wuhan 430074, China*

This paper has been typeset from a TEX/LATEX file prepared by the author.